AGU PUBLICATIONS

Geochemistry, Geophysics, Geosystems

RESEARCH ARTICLE
10.1002/2014GC005425

A Cenozoic uplift history of Mexico and its surroundings from longitudinal river profiles

Simon N. Stephenson[1], Gareth G. Roberts[1], Mark J. Hoggard[2], and Alexander C. Whittaker[1]

[1]Department of Earth Science and Engineering, Royal School of Mines, Imperial College London, London, UK, [2]Department of Earth Sciences, Bullard Laboratories, University of Cambridge, Cambridge, UK

Key Points:
- Admittance calculations indicate Te of plate beneath Mexico is ~11 km
- Admittance indicates that Mexican topography is dynamically supported by 1–2 km
- Inversion of river profiles shows dynamic support grew in the last 30 Ma

Correspondence to:
G. G. Roberts,
gareth.roberts@imperial.ac.uk

Citation:
Stephenson, S. N., G. G. Roberts, M. J. Hoggard, and A. C. Whittaker (2014), A Cenozoic uplift history of Mexico and its surroundings from longitudinal river profiles, *Geochem. Geophys. Geosyst.*, *15*, 4734–4758, doi:10.1002/2014GC005425.

Received 16 MAY 2014
Accepted 10 NOV 2014
Accepted article online 17 NOV 2014
Published online 9 DEC 2014

Abstract Geodynamic models of mantle convection predict that Mexico and western North America share a history of dynamic support. We calculate admittance between gravity and topography, which indicates that the elastic thickness of the plate in Mexico is 11 km and in western North America it is 12 km. Admittance at wavelengths > 500 km in these regions suggests that topography is partly supported by subcrustal processes. These results corroborate estimates of residual topography from isostatic calculations and suggest that the amount of North American topography supported by the mantle may exceed 1 km. The Cenozoic history of magmatism, sedimentary flux, thermochronometric denudation estimates, and uplifted marine terraces imply that North American lithosphere was uplifted and eroded during the last 30 Ma. We jointly invert 533 Mexican and North American longitudinal river profiles to reconstruct a continent-scale rock uplift rate history. Uplift rate is permitted to vary in space and time. Erosional parameters are calibrated using incision rate data in southwest Mexico and the Colorado Plateau. Calculated rock uplift rates were 0.15–0.2 mm/yr between 25 and10 Ma. Central Mexico experienced the highest uplift rates. Central and southern Mexico continued to uplift at 0.1 mm/yr until recent times. This uplift history is corroborated by independent constraints. We predict clastic flux to the Gulf of Mexico and compare it to independent estimates. We tentatively suggest that the loop between uplift, erosion, and deposition can be closed here. Mexico's staged uplift history suggests that its dynamic support has changed during the last 30 Ma.

1. Introduction

Geodynamic models, which use seismic velocities to estimate a history of mantle convection, predict that Mexico and western North America share a history of dynamic support [e.g., *Spasojevic et al.*, 2008; *Liu and Gurnis*, 2010; *Flament et al.*, 2013]. In western North America, slow velocity anomalies in surface wave tomographic models, clumped-isotope palaeoaltimetry, thermochronometry, rare Earth element geochemistry, and joint inversion of drainage networks have convincingly shown that the Cenozoic history of uplift there is related to mantle convection [e.g., *Fitton et al.*, 1991; *Humphreys et al.*, 2003; *Karlstrom et al.*, 2008; *Huntington et al.*, 2010; *Roberts et al.*, 2012; *Flowers and Farley*, 2012].

Uplifted marine terraces, the history of magmatism and river incision, and thermochronometric data show that Mexico and its surroundings have been uplifted by > 1 km and eroded since 50 Ma [e.g., *Righter*, 1997; *Gray et al.*, 2003; *Montgomery and Lopez-Blanco*, 2003; *Righter et al.*, 2010; *Ferrari et al.*, 2012]. Widespread, flat-lying, post-Paleocene sedimentary stratigraphy indicate that surface strain rates have been low during this time, which is consistent with thermobarometric studies that indicate lithospheric shortening ceased at ~50 Ma [e.g., *Suter*, 1984; *Gray et al.*, 2003; *Barra et al.*, 2005]. These observations suggest that dynamic support might have played a role in generating its topography.

In this paper, we estimate the uplift history of Mexico and southwestern U.S., including the Colorado Plateau. We quantify the extent that their histories of uplift can be explained by changing patterns of mantle (e.g., dynamic) support. First, we estimate the present-day dynamic support of Mexico by calculating the transfer function between topography and gravity (admittance) for a region centered on the Mexican Altiplano. Results are compared to admittance calculated for an area centered on the Colorado Plateau and to simple isostatic calculations. Second, we estimate the history of rock uplift in Mexico and western North America by jointly inverting 533 longitudinal river profiles for uplift rate. We use a calibrated advection-diffusion scheme to model fluvial erosion. This approach allows us to reconcile independent thermochronometric, surface heat flow, incision, and uplift data.

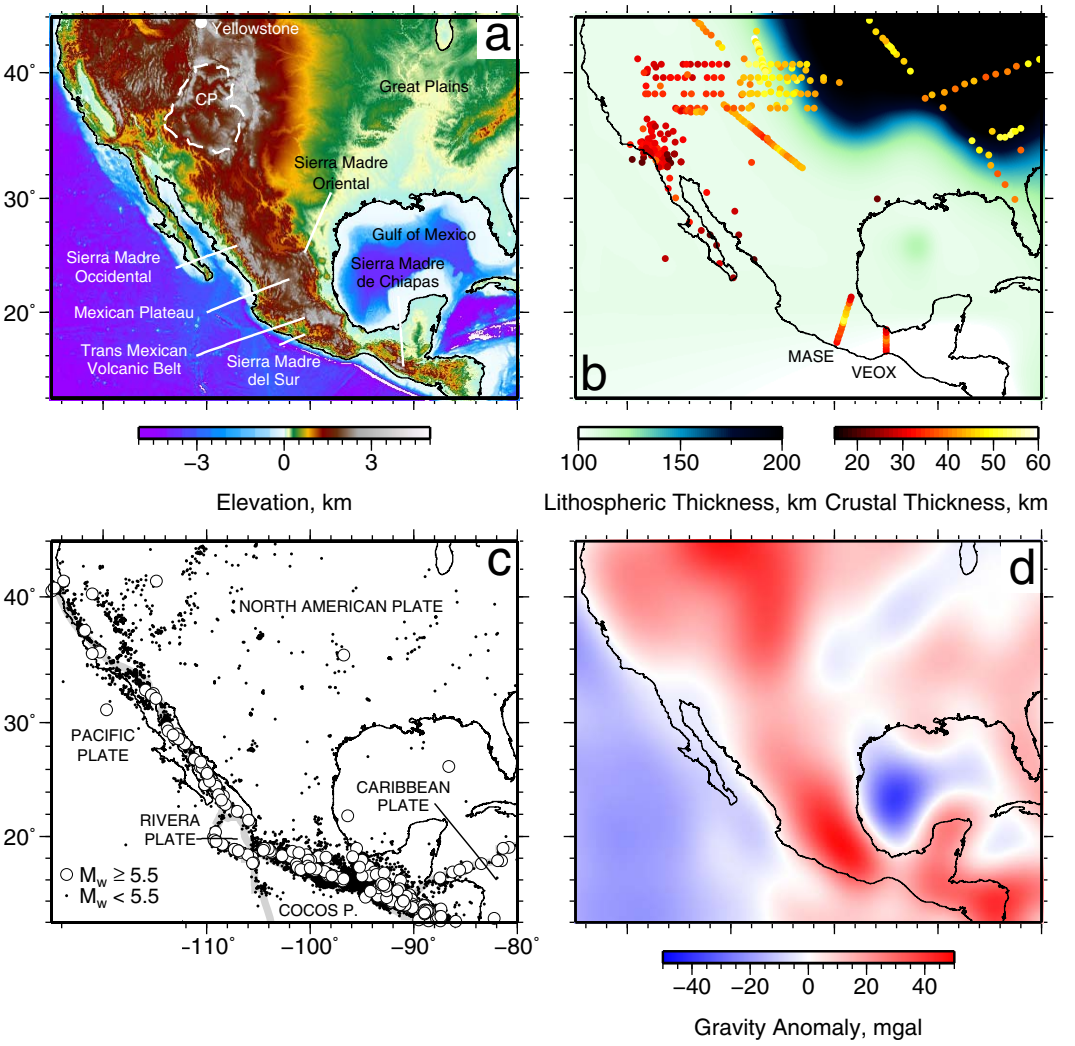

Figure 1. (a) Topographic map (ETOPO1). (b) Contours = lithospheric thickness [*Priestley and McKenzie*, 2006]. Circles = crustal thickness data from MASE and VEOX experiments and United States [*Braile*, 1989; *Sheehan et al.*, 1995; *Snelson et al.*, 1998; *Li et al.*, 2002; *Wilson et al.*, 2005; *Persaud et al.*, 2007; *Perez-Campos et al.*, 2008; *French et al.*, 2009; *Melgar and Perez-Campos*, 2010]. (c) Seismic data and plate boundaries. Seismic data from the USGS data set between 20 December 2000 and 20 December 2013. (d) Long-wavelength (800–2500 km) free air gravity anomalies [*Tapley et al.*, 2005].

1.1. Geophysical and Geomorphic Framework

Mexican topography is characterized by broad, high-elevation, and low-relief plains. The Sierra Madre Occidental, Mexican Altiplano, Trans-Mexican Volcanic Belt and Sierra Madre del Sur are 1–3 km high and are deeply incised by families of drainage networks (Figure 1a). The Sierra Madre Occidental and Oriental mountain chains in the west and east, respectively, bound the low-relief Mexican Altiplano, which is on average $\sim$ 1.8 km high. In the south, the Trans-Mexican Volcanic Belt has peaks $>$ 5 km and is the highest region in Mexico. In contrast, eastern Mexico is predominantly a low-elevation and low-relief coastal plain drained by eastward flowing rivers.

Receiver functions calculated using the MARS, MASE, and VEOX arrays show that the crust in southern Mexico is approximately 18–20 km thick at the coast and up to 50 km thick inland (Figure 1b) [*Perez-Campos et al.*, 2008; *Melgar and Perez-Campos*, 2010; *Kim et al.*, 2011]. Conversion of surface wave tomographic models to temperature indicates that the lithosphere beneath this region is unlikely to be more than 100 km thick (Figure 1b) [*Priestley and McKenzie*, 2006]. These results are consistent with other surface wave studies, which show that the lithospheric mantle beneath Mexico is not thick [e.g., *Grand*, 1994; *Bijwaard and Spakman*, 2000; *Ritsema et al.*, 2004]. Slow seismic wave speeds suggest that the asthenosphere beneath Mexico is hotter than its surroundings and buoyant [e.g., *Goes and van der Lee*, 2002; *French et al.*, 2013]. Earthquake

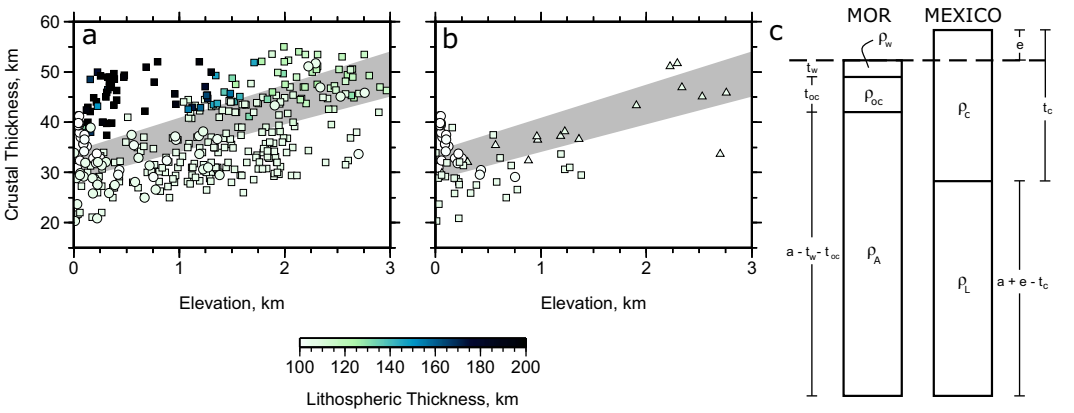

Figure 2. Crustal thickness and elevation. (a) Circles and squares = crustal thicknesses and elevations in Mexico and United States, respectively. Elevation extracted from ETOPO1 data set, averaged over 5 min. Colors = lithospheric thickness (Figure 1b). Gray envelope = elevation for an isostatically balanced column of lithosphere which has a crustal thickness of 30 km and density, $\rho_c = 2.75 \pm 0.05 g/cm^3$. (b) Mexican data only. Circles = VEOX array; triangles = MASE array; squares = Baja California [*Perez-Campos et al.*, 2008; *Melgar and Perez-Campos*, 2010; *Kim et al.*, 2011]. (c) Isostatic model: (left) mid-oceanic ridge; (right) local conditions; $t_w = 2.3$ km, $\rho_w = 1$ g/cm^3, $t_{oc} = 7$ km, $\rho_{oc} = 2.9$ g/cm^3, $\rho_A = 3.2$ g/cm^3, $\rho_L = 3.3$ g/cm^3, and $a = 100$ km.

epicentres define the location of the Mid-America subduction zone and the Cocos-Caribbean-North American triple junction in southwest Mexico (Figure 1c) [*Ferrari et al.*, 2002]. Body waveform modeled earthquakes in central Mexico typically have normal focal mechanisms, which suggests that this region is extending [e.g., *Pardo and Suárez*, 1995; *Suter et al.*, 2001].

In central and southern Mexico, long-wavelength free-air gravity anomalies (+ 45 mGal) are centered on the Trans-Mexican Volcanic Belt. Further north (~30°N) gravity anomalies decrease to + 5 mGal and in western North America, a long wavelength, + 30 mGal, free-air gravity anomaly is centered on Yellowstone and encompasses the Colorado Plateau (Figure 1d) [e.g., *Tapley et al.*, 2005]. Long-wavelength positive free-air gravity anomalies indicate that topography is not supported solely by crustal isostasy. Tomographic models and receiver function studies in western North America show that its positive free-air gravity anomalies are likely to be associated with hot and low-density mantle that supports topography [e.g., *Wilson et al.*, 2005; *Ritsema et al.*, 2011; *French et al.*, 2013]. In the following section, we use simple isostatic calculations and the transfer function between gravity and topography to estimate the amplitude of dynamic support of western North America and Mexico.

2. Admittance Between Gravity and Topography

2.1. Crustal Isostasy

Figure 2 shows elevations compared to crust and lithospheric thickness estimates from receiver function, wide angle, and surface wave studies in western North America and Mexico [e.g., *Gilbert et al.*, 2003; *Gilbert and Sheehan*, 2004; *Wilson et al.*, 2005; *Priestley and McKenzie*, 2006]. Figure 2b shows crustal thickness from 63 receiver function experiments in southern Mexico (MASE, VEOX) [*Perez-Campos et al.*, 2008; *Melgar and Perez-Campos*, 2010; *Kim et al.*, 2011]. A striking observation is that the relationship between crustal thickness and elevation is weak in both regions. By balancing the pressure at the base of a continental lithospheric column against a mid-oceanic ridge, the crustal thickness required to support observed topography isostatically can be estimated. Elevation, e, as a function of crustal thickness, t_c, for an isostatically compensated lithospheric column, can be expressed as

$$e = \frac{t_w(\rho_w - \rho_A) + t_{oc}(\rho_{oc} - \rho_A) + a(\rho_A - \rho_L) - t_c(\rho_c - \rho_L)}{\rho_L}. \quad (1)$$

The gray bands in Figure 2 show predicted elevation for a range of crustal densities from 2.7 to 2.8 g/cm^3. In many areas of Mexico, observed topography is greater than that expected given measured crustal thicknesses. In some places, residual (e.g., dynamic) topography is at least 1 km. We now calculate the transfer

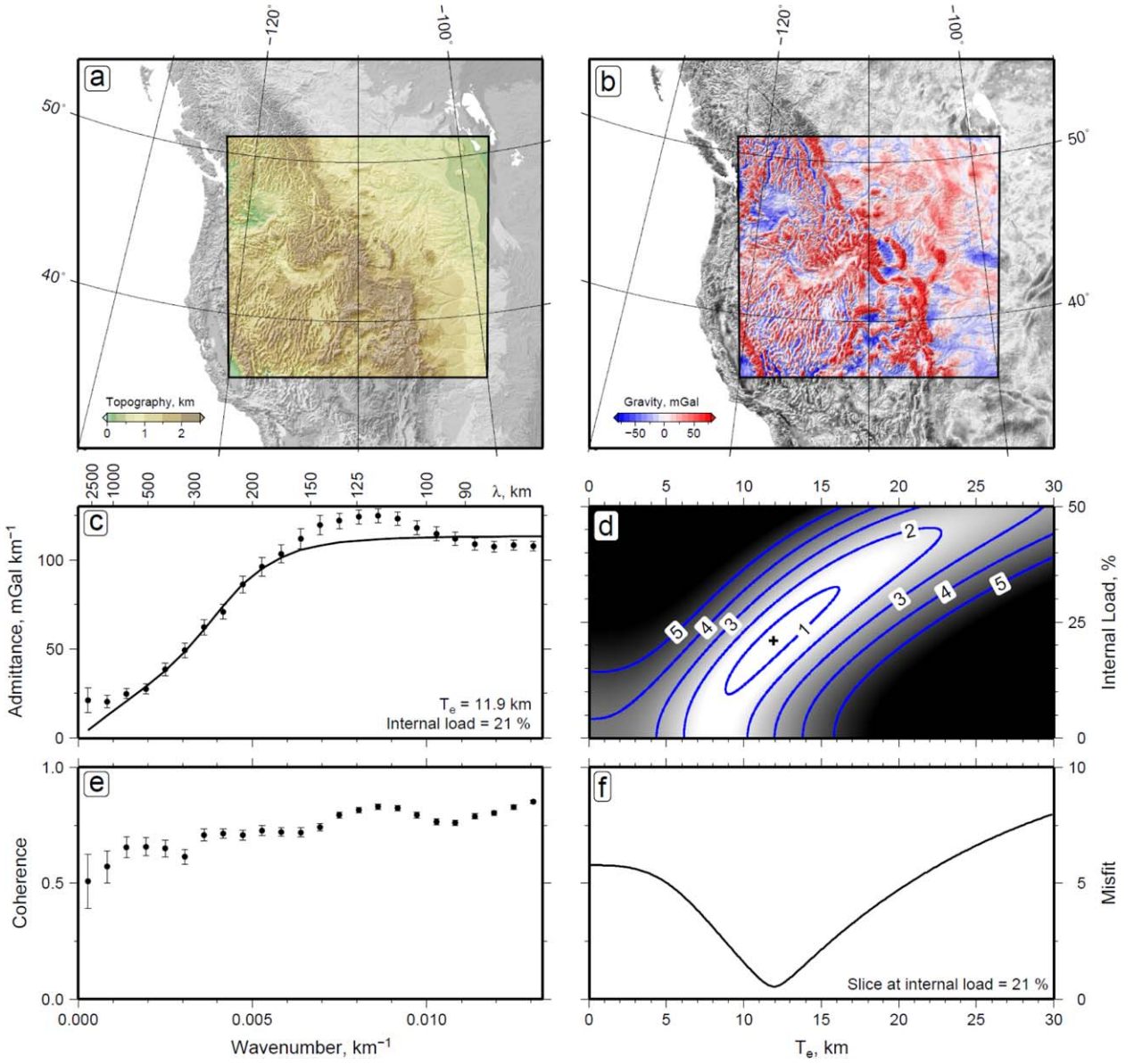

Figure 3. Admittance calculations for western U.S. (a) Box encloses topography used in calculation [*Becker et al*., 2009, SRTM30_PLUS]. (b) Unfiltered free air gravity anomaly from *Förste et al*. [2011, EIGEN6c]. (c) Admittance as a function of wave number; black line = best-fitting elastic model: T_e = 11.9 km. At long (> 1000 km) wavelengths, the elastic model fits the data poorly and admittance = 23 ± 5 mGal/km. (d) Misfit as a function of elastic thickness and internal loading. Best-fitting elastic model requires a 21% internal load. (e) Coherence between topography and free air gravity as function of wave number. (f) Slice through misfit well shown in Figure 3d at internal load = 21%.

function between free-air gravity and topography to estimate the amplitude of dynamic support of Mexico and western North America (Figures 3 and 4).

2.2. Admittance

The relationship between gravity, g, and topography, t, can be used to estimate the elastic thickness of the lithosphere, internal loading, and the amount of dynamic support [e.g., *McKenzie*, 2003]. If t is free from noise and g is affected by noise, this relationship, admittance, Z, as a function of wave number, $k = 2\pi/\lambda$, can be expressed as

$$Z = \frac{<\bar{g}\bar{t}^{*}>}{<\bar{t}\bar{t}^{*}>} \tag{2}$$

where $\bar{g}$ and $\bar{t}$ are multitaper Fourier transforms of gravity and topography data. Angular brackets denote the average value over wave number bands and the asterisks denote complex conjugates [*McKenzie and Fairhead*, 1997].

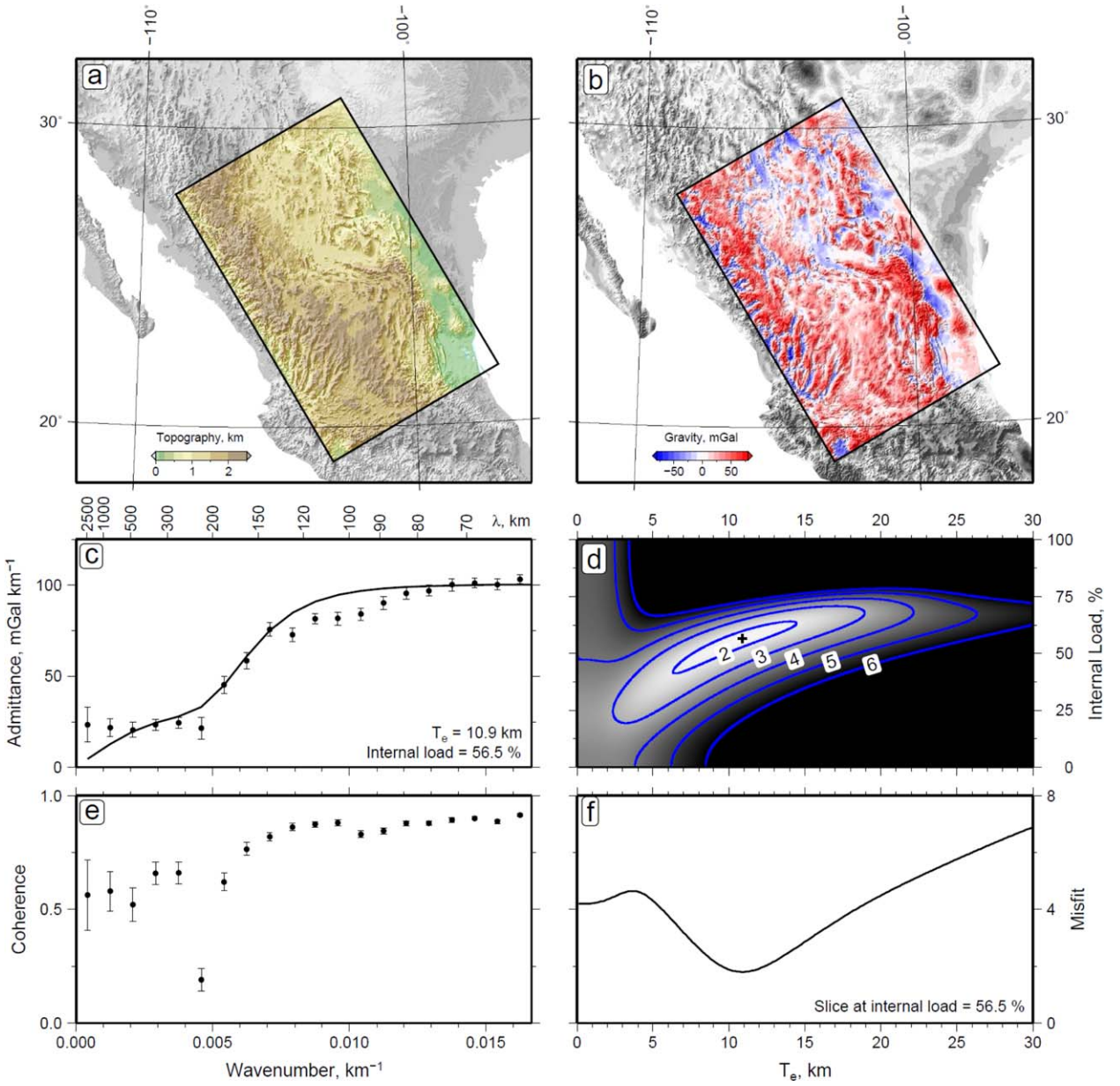

Figure 4. Admittance calculation for Mexico. (a) Box encloses topography used in calculation. (b) Unfiltered free air gravity anomaly. (c) Admittance as a function of wave number; black line = best-fitting elastic model: T_e = 10.9 km. At long (> 1000 km) wavelengths admittance = 24 ± 7 mGal/km. (d) Misfit as a function of elastic thickness and internal loading. Best-fitting elastic model requires internal load of 56.5%. (e) Coherence between topography and free air gravity as a function of wave number. (f) Slice through misfit well shown in Figure 4d at internal load = 56.5%.

Figures 3 and 4 show the admittance between the EIGEN6c gravity data set and SRTM30_PLUS topography model for western North America and Mexico, respectively [*Becker et al.*, 2009; *Förste et al.*, 2011]. To determine the elastic model that best fits those data, we ran a suite of tests in which internal loading, elastic thickness, T_e, and plate density were varied. In these models, upper and lower crustal thicknesses were 20 and 15 km, respectively. Crustal densities determine the value of admittance at short wavelengths. In the Mexican model, best-fitting upper and lower crustal densities were 2.4 and 2.7 g/cm^3, respectively. In western North America, the respective best-fitting upper and lower crust densities were 2.7 and 2.9 g/cm^3. Admittance at intermediate wavelengths (e.g., 150–500 km) is determined by the elastic thickness of the plate. Figures 3c and 4c show that the best-fitting elastic models have a thickness of 12 km in western North America and 11 km in Mexico. In Mexico, admittance at the longest wavelengths (1000–2500 km) is 24 ± 7 mGal/km, which is similar to the calculated range for western North America (23 ±5 mGal/km) and indicates that its

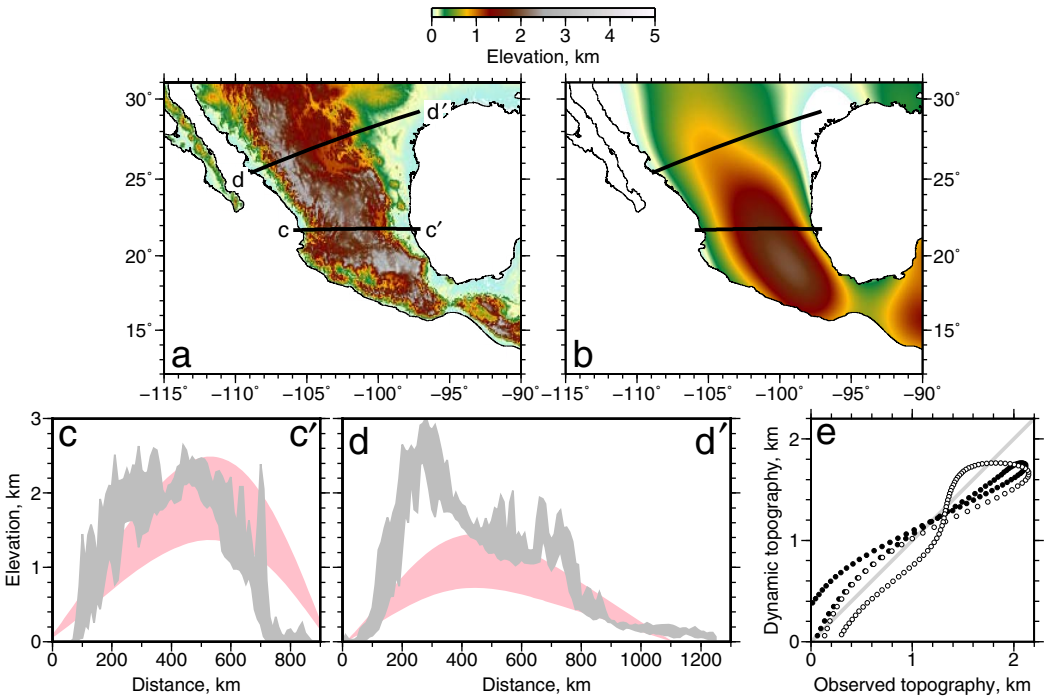

Figure 5. Dynamic topography in Mexico. (a) Observed topography. (b) Dynamic topography calculated using an admittance, *Z*, of 24 mGal/km (Figure 4c). (c and d) Pink band = dynamic topography for $Z = 24 \pm 7$mGal/km along swath shown in Figure 5a; gray band = minimum and maximum topography within 100 km of swath. (e) Median of observed topography filtered to remove wavelengths less than ~400 km compared to dynamic topography, $Z = 24$ mGal/km; gray line shows 1:1 relationship; filled circles = swath c−c′: Pearson's $r = 0.97$; unfilled circles = d−d′: $r = 0.96$.

topography is partially supported dynamically [e.g., *McKenzie*, 2010; *Jones et al.*, 2012]. The best-fitting elastic model for western North America requires an internal load of ~21% (Figure 3d). The best-fitting model for Mexico has an internal load of ~55% (Figure 4d). This load could be generated by a dense and thick crustal root, which is consistent with high seismic velocities in the lower crust beneath Mexico observed in surface wave experiments [*Bonner and Herrin*, 1999]. The coherence, a measure of the strength of the relationship between gravity and topography, is high (> 0.5) at nearly all wave number bins (Figures 3e and 4e).

To estimate the amplitude of dynamic support across Mexico, the EIGEN6c data set was filtered to remove wavelengths less than ~800 km and then divided by 24 mGal/km, the admittance at longest wavelengths. In central Mexico, predicted dynamic topography often has a similar elevation to observed topography (Figure 5c). In northwest Mexico, calculated dynamic topography is ~1 km less than observed topography, in the east it is more closely matched (Figure 5d). In regions that are dynamically supported, the uplift history of the Earth's surface contains important clues about the spatiotemporal evolution of the mantle. To constrain the history of dynamic support in Mexico, we now seek a history of uplift rate. First, we compile observations of uplift and denudation. We then place these independent observations into a framework by inverting the longitudinal profiles of 533 North American rivers.

3. Magmatism, Uplift, and Erosion

The most convincing evidence for Cenozoic uplift in western North America is the distribution of Cretaceous-Paleocene marine rocks that now crop out at elevations up to a few kilometers (Figure 6) [*Bond*, 1976; *Sahagian*, 1987]. The history of magmatism, sedimentary flux to the Gulf of Mexico, clumped-isotope palaeoalitmetry, measurements of incision, drainage patterns, and thermochronometric data indicate that western North America has undergone staged Cenozoic uplift [e.g., *Fitton et al.*, 1991; *Humphreys et al.*, 2003; *Karlstrom et al.*, 2008; *Huntington et al.*, 2010; *Galloway et al.*, 2011; *Roberts et al.*, 2012; *Flowers and Farley*, 2012].

In Mexico, the history of regional volcanism and 1–2 km of post-Oligocene fluvial incision of west coast ignimbrites are convincing evidence of Cenozoic uplift and denudation [e.g., *Righter*, 1997; *Montgomery and Lopez-Blanco*, 2003; *Ferrari et al.*, 2012]. The west coast was peppered by felsic magmatism during Eocene

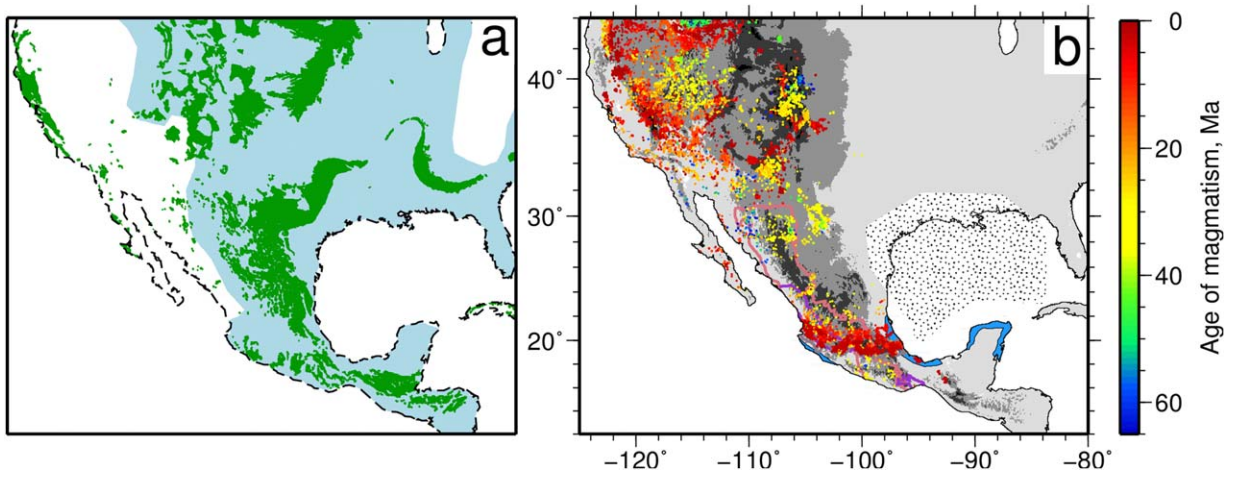

Figure 6. Cretaceous and Cenozoic palaeogeography of North America. (a) Creataceous palaeogeography. Green = outcropping Cretaceous sedimentary rocks, which typically have marine facies in western and central North America [*Reed et al*., 2005]. Blue = interior seaway at 90–70 Ma [e.g., *Bond*, 1976; *Sahagian*, 1987; *Smith et al*., 1994]. Dashed line = modern coastline. (b) Cenozoic palaeogeography. Gray scale = modern elevation contoured every 1 km; black = elevations $\geq$ 2 km (ETOPO1). Note 1–3 km elevation of Cretaceous marine rocks in western North America and Mexico today. Circles = magmatism colored for age [*Ferrari et al*., 1999, 2007; www.navdat.org]. Pink and purple polygons = respective distribution of Oligocene and Miocene ignimbritic rocks in Mexico [*Ferrari et al*., 1999; *Stevens and Stevens*, 2003; *Chapin et al*., 2004]. Stippled pattern = clastic deposition in the Gulf of Mexico, which increased dramatically at ~65 Ma [*Galloway et al*., 2000, 2011; *Alzaga-Ruiz et al*., 2009]. Blue polygons = uplifted Holocene marine terraces in Mexico [*Kim et al*., 2011].

and Oligocene times and dramatic Oligocene and Miocene ignimbrite flareups occurred throughout the Sierra Madre Occidental (Figure 6b) [*McDowell and Clabaugh*, 1979; *Ferrari et al*., 2002, 2007]. $^{40}Ar/^{39}Ar$ dating of mafic magmatism indicates that volcanism migrated southward from the Sierra Madre Occidental to the Trans-Mexican Volcanic Belt during Miocene times [*Ferrari et al*., 1999, 2002]. Rare Earth element depletion patterns show that magmas with an ocean-island-basalt affinity have been erupted throughout the Trans-Mexican Volcanic Belt during the last 20 million years [*Marquez et al*., 1999]. Hot, upwelling mantle likely generated those basalts and uplifted the Earth's surface [*Ferrari et al*., 2001, 2007, 2012]. Sedimentary flux into the western Gulf of Mexico was high at that time [*Galloway et al*., 2011; ~10^5 km^3/Ma]. Apatite fission track and (U-Th)/He thermochronometric data from the Sierra Madre Oriental and Sierra Madre de Chiapas mountain ranges in central and southern Mexico require ~100°C of cooling between 40 and 15 Ma [*Gray et al*., 2003; *Witt et al*., 2012]. Quaternary marine terraces along the Jalisco and Colima coasts in southwest Mexico, and Veracruz in eastern Mexico are observed at elevations of a few 10 s of meters [*Self*, 1979; *Ramirez-Herrera et al*., 2010].

Independent measurements of uplift and erosion in Mexico are limited by their spatial resolution. Drainage networks, which are ubiquitous across the Earth's surface at low-mid latitudes, can act as tectonic "tape recorders" [e.g., *Rosenbloom and Anderson*, 1994; *Whipple and Tucker*, 1999; *Roberts and White*, 2010]. In the next section, we first show that the longitudinal profiles of North American rivers contain large knickzones and that they record a history of uplift. We place independent estimates of uplift into a regional framework by inverting those profiles.

4. Drainage Networks

We extracted 533 longitudinal river profiles from the 1 arc second (~30×30 m) ASTER Global Digital Elevation Map (DEM) and the SRTM DEM (~90×90 m) using Esri flow routing algorithms (Figure 7). The horizontal resolution of the ASTER GDEM is ~70 m and its absolute vertical error at the 95% confidence level is 17 m [*Meyer et al*., 2011]. Anomalous depressions and spikes in the DEM were first removed. Then the direction of flow and upstream drainage area were calculated. The extracted drainage network was compared to Landsat imagery to assess accuracy. The initiation of overland flow was identified for all rivers in our data set using Landsat imagery. Typically, overland flow occurs when $A > 10–20$ km^2. Drainage in the Sonoran and Chihuahuan deserts, northern Mexico, is absent or sometimes masked by sand-seas, elsewhere drainage recovery is generally good. The largest river draining Mexico is the Rio Grande, which drains northern

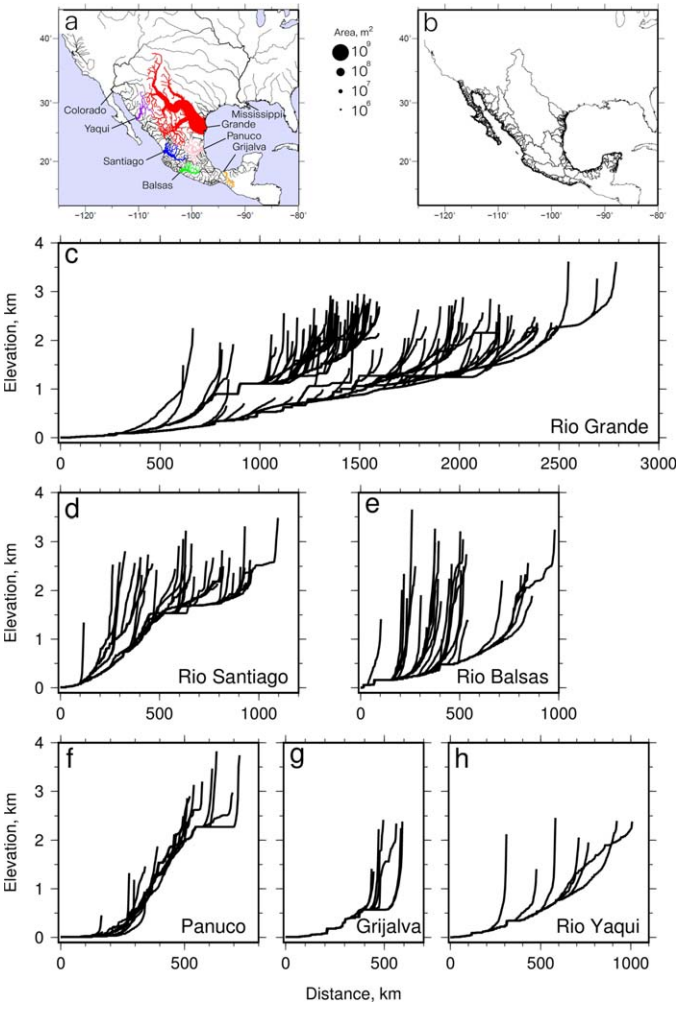

Figure 7. (a) Map of 533 rivers used in this study, which were extracted from ASTER and SRTM DEMs filled to remove anomalous spikes and sinks. Six largest Mexican catchments shown in (c–h). Width of colored Mexican rivers scaled to upstream drainage area. (b) Drainage divides. (c–h) Longitudinal profiles. Note knickzones exist in all catchments.

and central Mexico and large parts of southern U.S. (Figure 7c). Its source is located on the Colorado Plateau and a major tributary has its headwaters in the Sierra Madre Occidental, western Mexico. In southern Mexico, the largest basins are drained by Rio Grande de Santiago, Rio Balsas, and Rio Panuco (Figures 7d–7f).

4.1. What Controls the Shapes of Longitudinal River Profiles?

Knickzones up to 200 km wide exist on the Rio Grande and other large rivers in Mexico (Figure 7). To test whether these knickzones have been generated by changes in lithology, the elevation of the Rio Santiago, Rio Grande, and Rio Grijalva was compared to bedrock geology (Figure 8). The correlation between the position of lithological boundaries and knickzones is weak. This analysis is consistent with work by *Roberts et al*. [2012] who also found that there is a weak relationship between knickzone location and lithology on the Rio Grande.

Glacioeustasy can generate rapid (∼100 ka) base-level variations with amplitudes typically $<$ 100 m, which can create knickzones at the coast [e.g.,

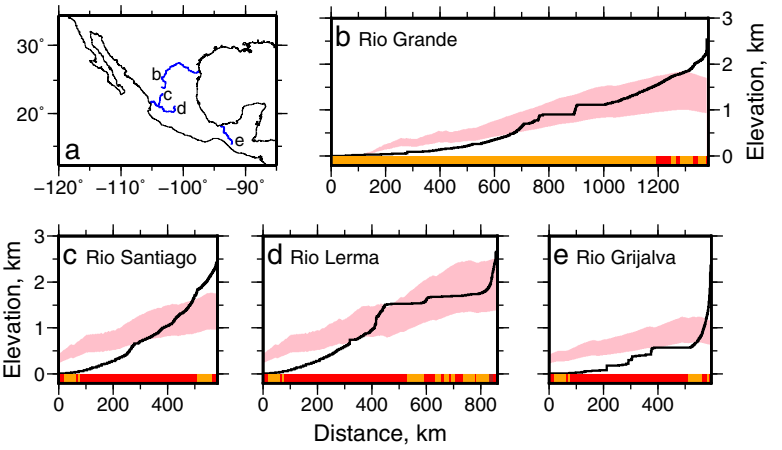

Figure 8. Dynamic topography and substrate lithology plotted along the length of selected rivers. Black line = longitudinal river profile; pink band = predicted dynamic topography using Admittance of 24 ± 7 mGal/km (Figure 4). Bottom bar shows substrate lithology: red = volcanic rocks; yellow = sedimentary rocks; purple = crystalline basement. Major knickzones along these river profiles do not correlate with lithological boundaries.

Miller et al., 2005]. However, these amplitudes are typically much smaller than convexities along Mexico's rivers (e.g., Figure 7). For simplicity, we assume that all rivers flow to a fixed sea-level.

In Figure 8, the longitudinal profiles of the Rio Santiago, Rio Grande, and Rio Grijalva are compared to predictions of dynamic support using an admittance of 24 ± 7 mGal/km (e.g., Figure 4). Large knickzones along these rivers have maximum elevations of 1–2 km, which is similar to the amplitude of calculated dynamic support in some places (Figures 8b–8e, pink bands). This figure suggests that shapes of longitudinal river profiles in Mexico are governed by uplift generated by subcrustal processes, and that erosion plays a moderating role. In the next section, we quantify the history of uplift through time by inverting these longitudinal river profiles.

5. River Profile Evolution

The rate of change of elevation, $\partial z/\partial t$, along a river is determined by the history of uplift rate, $U(x, t)$, and erosion rate, $E(x, t)$, where x and t are distance from the head of the river and time, respectively, and so

$$\frac{\partial z}{\partial t} = U(x,t) + E(x,t). \tag{3}$$

To determine the evolution of a longitudinal river profile, E must be parameterized. In this study, we use a stream power law, which assumes that E varies as a function of discharge [e.g., *Hack*, 1957]. Upstream drainage area, A, is used as a proxy for discharge. This assumption leads to the well-documented equation

$$E(x,t) = -vA(x)^m \left(\frac{\partial z}{\partial x}\right)^n + \kappa\left(\frac{\partial^2 z}{\partial x^2}\right) \tag{4}$$

where the prefactor, v, the area exponent, m and the slope exponent n are empirically derived constants and κ is erosional "diffusivity" [e.g., *Howard et al.*, 1994; *Rosenbloom and Anderson*, 1994]. The first term on the right-hand side of equation (4) determines the velocity of migrating knickzones and represents detachment-limited erosional processes [e.g., *Whipple and Tucker*, 1999; *Kirby and Whipple*, 2001]. The second term is diffusive and represents the transport-limited erosional system [e.g., *Whipple and Tucker*, 2002]. There is vigorous debate about the values of the erosional parameters, in particular n [*cf. DiBiase et al.*, 2010; *Roberts et al.*, 2012; *Lague*, 2014]. If $n \neq 1$, then shocks can develop, which can generate spatiotemporal gaps [*Pritchard et al.*, 2009; *Perron and Royden*, 2012]. However, recent field studies have indicated that $n \sim 1$ [e.g., *Whittaker et al.*, 2007; *Whittaker and Boulton*, 2012]. For simplicity, we initially assume that $n = 1$, this assumption will be tested in section 5.2. The erosional parameters v, m and n trade-off and different combinations can give similar knickzone retreat rates [e.g., *Stock and Montgomery*, 1999; *Berlin and Anderson*, 2007; *Roberts and White*, 2010]. Our approach is deliberately simple: more complex erosional models exist, but it is more profitable to thoroughly test simple schemes before introducing extra complexity, especially when considering timescales of $10^6 - 10^7$ years. The values of erosional parameters must be calibrated using independent geologic information.

If erosional "diffusion" is unimportant and $U = 0$, equations (3) and (4) can be rearranged so that

$$v = A^{-m}\frac{\partial z}{\partial t}\left(\frac{\partial z}{\partial x}\right)^{-n}. \tag{5}$$

Uncertainty in v, δv, can be estimated by propagating errors through equation (5) so that

$$\frac{\delta v}{|v|} = \sqrt{\left(\frac{\delta(\partial z/\partial t)}{|\partial z/\partial t|}\right)^2 + \left(\frac{|-n|\delta(\partial z/\partial x)}{|\partial z/\partial x|}\right)^2 + \left(\frac{|-m|\delta(A)}{|A|}\right)^2}. \tag{6}$$

Roberts et al. [2012] used the rate of incision recorded by eroded basalt dams in the Grand Canyon to calibrate erosional parameter values [$\partial z/\partial t = 111 \pm 7$ m/Ma; see *Karlstrom et al.*, 2008]. They incorporated errors in slope and area and found that $v = 203 \pm 25$ m$^{0.6}$/Ma when $n = 1$ and $m = 0.2$. In southwestern Mexico, the incision history of ignimbrites can be used to place broad estimates on the values of erosional parameters. *Montgomery and Lopez-Blanco* [2003] determined an average incision rate, $\partial z/\partial t$, of 110 ±37 m/Ma during the last 19.5 ± 6.5 Ma, and measured slopes, $\partial z/\partial x$, of 0.00218 ±0.00113 along a tributary of the Rio Santiago, where its upstream area is $A = 1.3 \times 10^{10}$ m^2. If slope has remained constant and $m = 0.2$ and $n = 1$,

then $v = 203^{+579}_{-23}$ m$^{0.6}$/Ma, which overlaps with the narrower range of values determined for the Colorado Plateau. Armed with erosional parameter values, we can now estimate landscape response times.

5.1. Landscape Response Time

If $n = 1$ and transport due to advection is much larger than that due to erosional "diffusion" (i.e., $vA^m/\kappa \gg 1$), then equation (4) can be rearranged and integrated to give the time taken for a knickzone to propagate from the mouth of the river to any point, x along the river

$$\tau_G = \int_{\circ}^{x} \frac{dx}{vA^m}, \tag{7}$$

where τ_G is the Gilbert (i.e., landscape response) time [e.g., *Whipple and Tucker*, 1999; *Whipple*, 2001; *Roberts et al.*, 2012]. Plots of τ_G are a useful guide for assessing the length of time that drainage networks could resolve different uplift events. The value of m determines the spatial distribution of migrating knickzones in a drainage network. v sets the timescale of knickzone propagation. Figure 9 shows that if $m = 0.2$ and $v = 200$ m$^{0.6}$/Ma Mexican drainage networks have the potential to resolve uplift events during the last 90 Ma. As is evident from equation (7), larger values of v reduce calculated response times along a river and smaller values increase them. *Willett et al.* [2014] and *Shelef and Hilley* [2014] have argued that differences between response times across drainage divides mean that drainage topology must be evolving in time and space. Close to drainage divides, the recording time increases dramatically because upstream drainage area becomes very small so the theoretical knickzone migration rate drops rapidly. In this region, hillslope processes also dominate erosion. Additionally, apparent discrepancies between response times can be artifacts generated by the use of discrete digital elevation data (e.g., Figure 9). It is unclear how these issues affect the results of *Willett et al.* [2014] and *Shelef and Hilley* [2014]. More widely, the extent to which drainage topologies are highly dynamic in time at regional to continental scales is unknown [e.g., *Cowie et al.*, 2006].

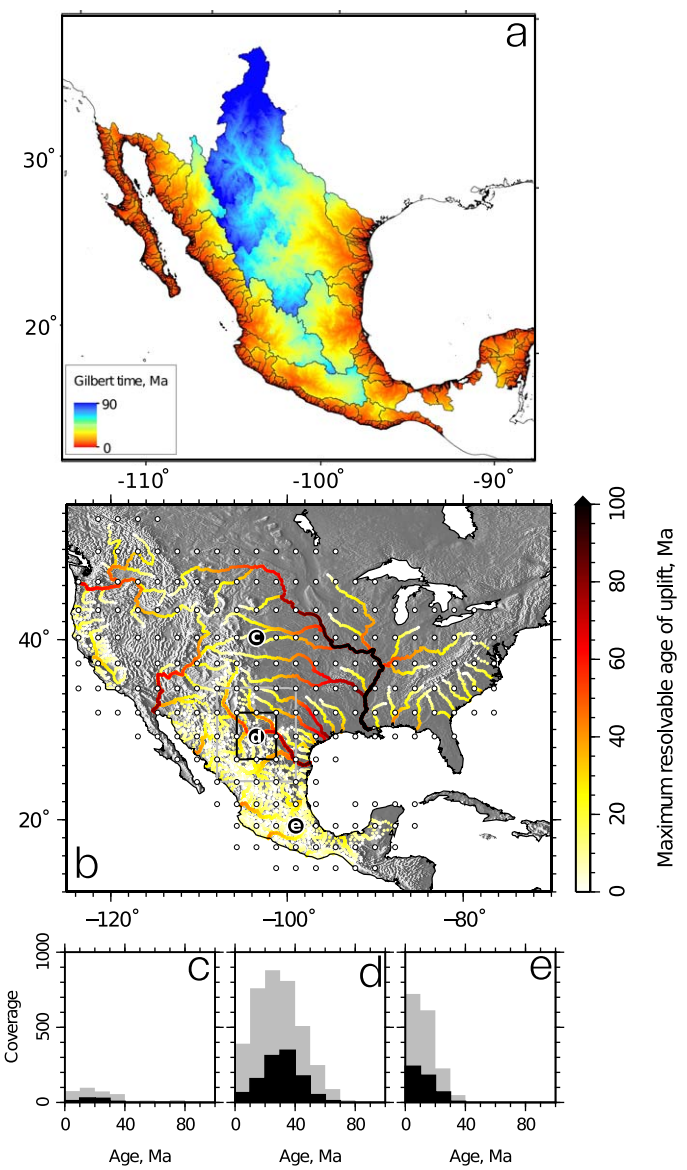

Figure 9. (a) Gilbert (landscape response) time, τ_G, for catchments in Mexico (see equation (7)). Black lines = loci of drainage divides; τ_G contour interval = 5 Ma. τ_G at the headwater of the Rio Grande is ~90 Ma. (b) Resolvable age of uplift in North America, which is directly related to τ_G. White circles are evenly spaced every 250 km. (c–e) Gray histograms show model coverage when data set is sampled in 1000 km bins (see gray box in Figure 9b); black histograms = 500 km sampling (see black box in Figure 9b). Figure 9b shows location of Figures 9c–9e.

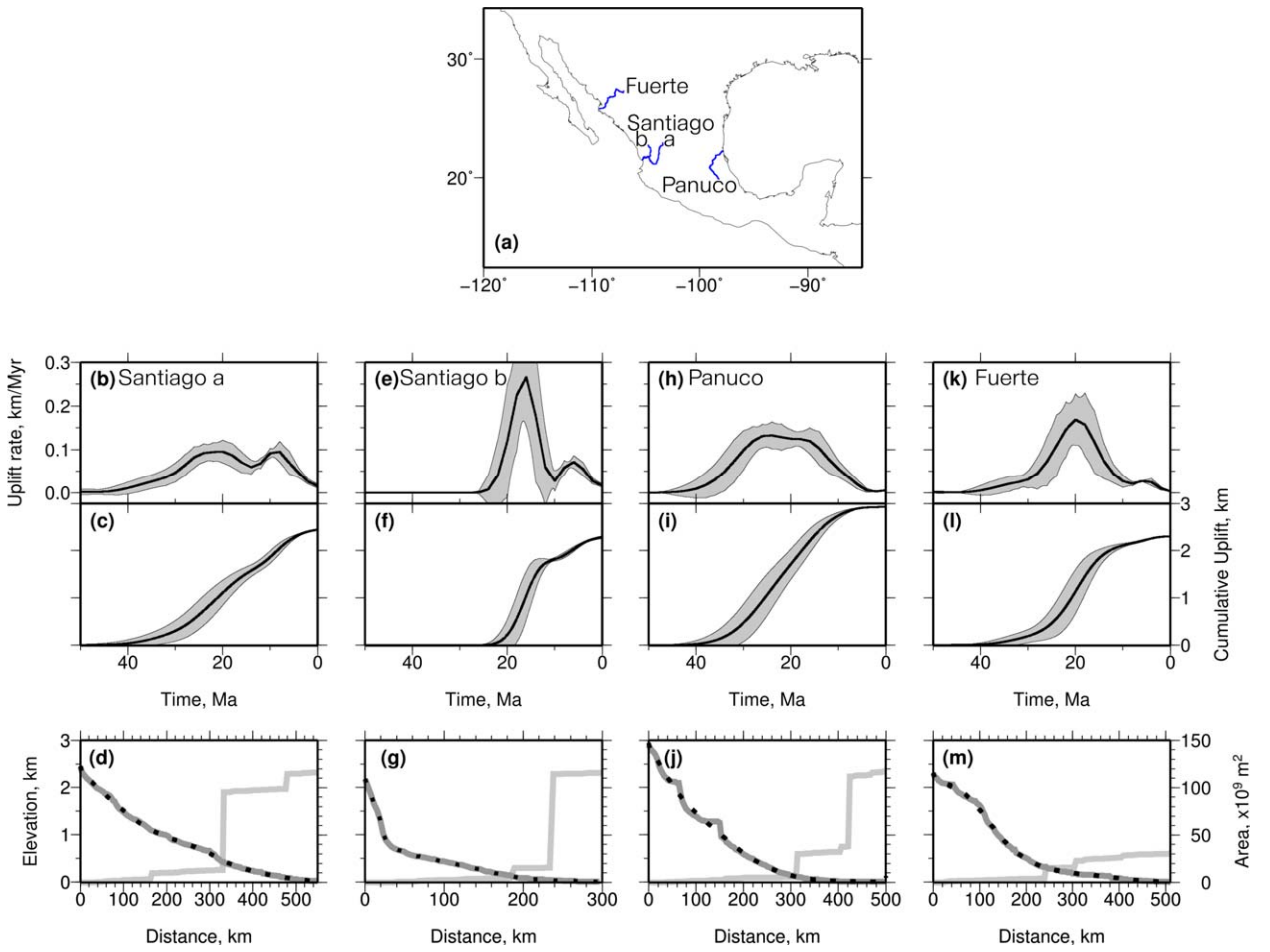

Figure 10. Inverting for uplift as function of time, $U(t)$. (a) Map shows rivers inverted. Erosional parameters were randomly varied within bounded ranges in 50 inversions: $200 \leq v \leq 210, 0.19 \leq m \leq 0.21, 1 \leq n \leq 1.05, 10^2 \leq \kappa \leq 10^3$. (b) Calculated uplift rates for Rio Grande de Santiago. Black line = average uplift rate history, gray bands = 1σ uncertainty. (c) Cumulative uplift (i.e., $\int_0^t U(t)\mathrm{d}t$). Black line = average cumulative uplift history, gray band = 1σ uncertainty. (d) Dark gray curve = observed longitudinal river profile of Rio Grande de Santiago; black dots = best fitting theoretical river profile; light gray line = upstream drainage area. (e–g) Tributary of Rio Grande de Santiago. (h–j) Rio Panuco. (k–m) Rio Fuerte.

Consequently, in the following section, we test the effect of varying upstream area on the timescale of calculated uplift.

5.2. Uplift as a Function of Time

Initially we invert for uplift rate solely as a function of time [e.g., *Pritchard et al.*, 2009; *Roberts and White*, 2010]. We seek the smoothest uplift rate history that yields the smallest misfit between calculated and observed river profiles. In this model, all knickzones originate at the mouth and propagate upstream at a rate related to upstream drainage area (equation (4); Figure 9b–9e). Given that the wavelength of dynamic support in Mexico is likely to be $>$ 500 km, we have focussed on inverting short rivers ($<$ 500 km) that drain to the coast (Figure 4). We inverted two tributaries of Rio Grande de Santiago, central Mexico, which were included in *Montgomery and Perez-Blanco's* [2003] study. We also inverted tributaries of Rio Fuerte and Rio Panuco, which drain north and south Mexico, respectively (Figure 10). *Powell*'s [1964] method, a conjugate-gradient scheme, was used to minimize

$$H = \left[\frac{1}{N}\sum_{i=1}^{N}\left(\frac{z_i^o - z_i^c}{\sigma_i}\right)^2\right]^{\frac{1}{2}} + w_1 f + \mu||m||, \tag{8}$$

by varying U [*Roberts and White*, 2010]. The first term on the right-hand side of equation (8) determines the root-mean-square (rms) misfit between observed and theoretical river profiles. N is the number of data points along the river profile. z_i^o and z_i^c are observed and calculated elevations, respectively, and σ_i is data

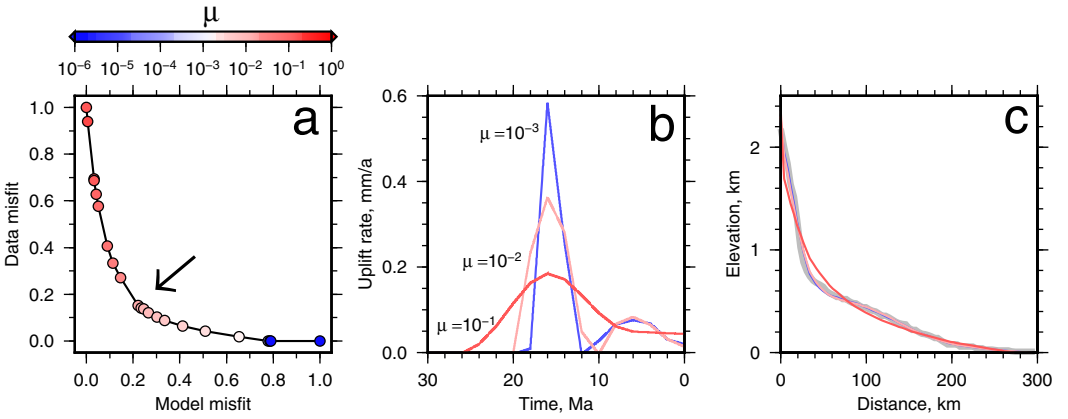

Figure 11. Testing regularization parameters. Inverting Rio Santiago for $U(t)$. (a) Circles = residual data misfit as a function of model misfit for range of values of regularization parameter, μ. Model misfit is a measure of $U(t)$ roughness (see equation (8)). Value of μ was chosen so that $U(t)$ is the smoothest model that best fits the data (arrow, $\mu=10^{-2}$) [*Parker*, 1994]. (b) Best fitting rock uplift rate histories for sweep of μ values. (c) Gray line-= observed longitudinal profile of Rio Santiago. Red, pink, blue lines show best fitting theoretical rivers when $\mu=10^{-1}, 10^{-2}, 10^{-3}$, respectively.

variance. The second term is a positivity constraint (i.e., $f=\cosh(U)-1$ when $U<0$, and $f=0$ when $U\geq 0$). The third term is a penalty function whose value depends on the first and second derivatives of $U(t)$, which ensures model smoothness and stabilises the inversion. The value of the regularization parameter, μ, determines model roughness, $||m||$. For each river, we performed a Monte Carlo bootstrap analysis. We randomly and independently varied erosional parameter values between $200\leq v\leq 210, 0.19\leq m\leq 0.21, 1\leq n\leq 1.05, 10^2\leq\kappa\leq 10^3$ in 50 inversions to assess how uncertainty in erosional parameter values map to uncertainty in calculated uplift. Results indicate that all four rivers were uplifted between 16 and 22 Ma at rates of 0.1–0.3 mm/yr. Rivers draining the Rio Grande de Santiago catchment also record a younger and smaller amplitude uplift event (Figure 10). The value of μ was chosen using *Parker* [1994]'s iterative method and in these models $\mu=10^{-2}$ (Figure 11).

An advantage of using an inverse approach is that model parameters can be systematically varied to determine their effect on residual misfit. In Figure 12, we show results from joint inversion of a family of four rivers in the Rio Grande de Santiago catchment for $U(t)$. We systematically varied n between 0.6 and 1.5. Erosional parameters were covaried using equation (5): if $n=1$, then $v\approx 4.16\times10^4(2.78\times10^{-12})^m$. We assigned μ a value of 10^{-2}. Each model was run for 50 million years. If shocks develop, rivers can erase part of their uplift history. Nonetheless, we find that rivers draining central Mexico are best fit when $n=1$. Figure 13 shows how covarying m and v for one tributary affects calculated uplift for Rio Grande de Santiago. Residual misfit is smallest when $0.1<m<0.4$ (Figures 13a–13g). *Rosenbloom and Anderson* [1994] estimate that diffusivity, $\kappa\sim 10^4\mathrm{m}^2/\mathrm{Ma}$. Figures 13h–13n show that changes in κ have a negligible effect on calculated uplift rate history or residual misfit when $\kappa<10^8\mathrm{m}^2/\mathrm{Ma}$ as is expected since our data has a resolution of ~20 km. For our purposes, erosional "diffusion" can be safely ignored. If the upstream area of the Rio Grande de Santiago is varied by ±50% since 50 Ma, the onset of calculated uplift is shifted by ±5 Ma (Figures 13o–13u).

So far we have assumed that fluvial discharge is a function of upstream drainage area. Discharge must also vary as a function of precipitation rate, which might adversely affect the reliability of our results. North America has remained at midlatitudes since Cretaceous times and has not migrated across major latitudinal climate zones [e.g., *Parrish et al.*, 1982]. Nonetheless, the distribution of Cenozoic eolian, fluvial, and lacustrine rocks suggests that its climate has been arid and wet coeval with growth and decay of ice sheets in the northern and southern hemispheres [e.g., *Cather et al.*, 2008]. At present, mean annual precipitation varies between <100 and >1500 mm across the continent; the west is generally much drier than the east [*Daly et al.*, 2008; 1971–2001 average]. In Mexico, coastal regions tend to be wetter than the interior. A pragmatic way to test the sensitivity of our results to different precipitation scenarios is to modify the erosional model so that

$$E=-v_\circ Q^m\frac{\partial z}{\partial t}, \tag{9}$$

where discharge, $Q(x, t)$, is the product of upstream drainage area, A, and precipitation rate, p [e.g., *Roe et al.*, 2002]. Here we assume that

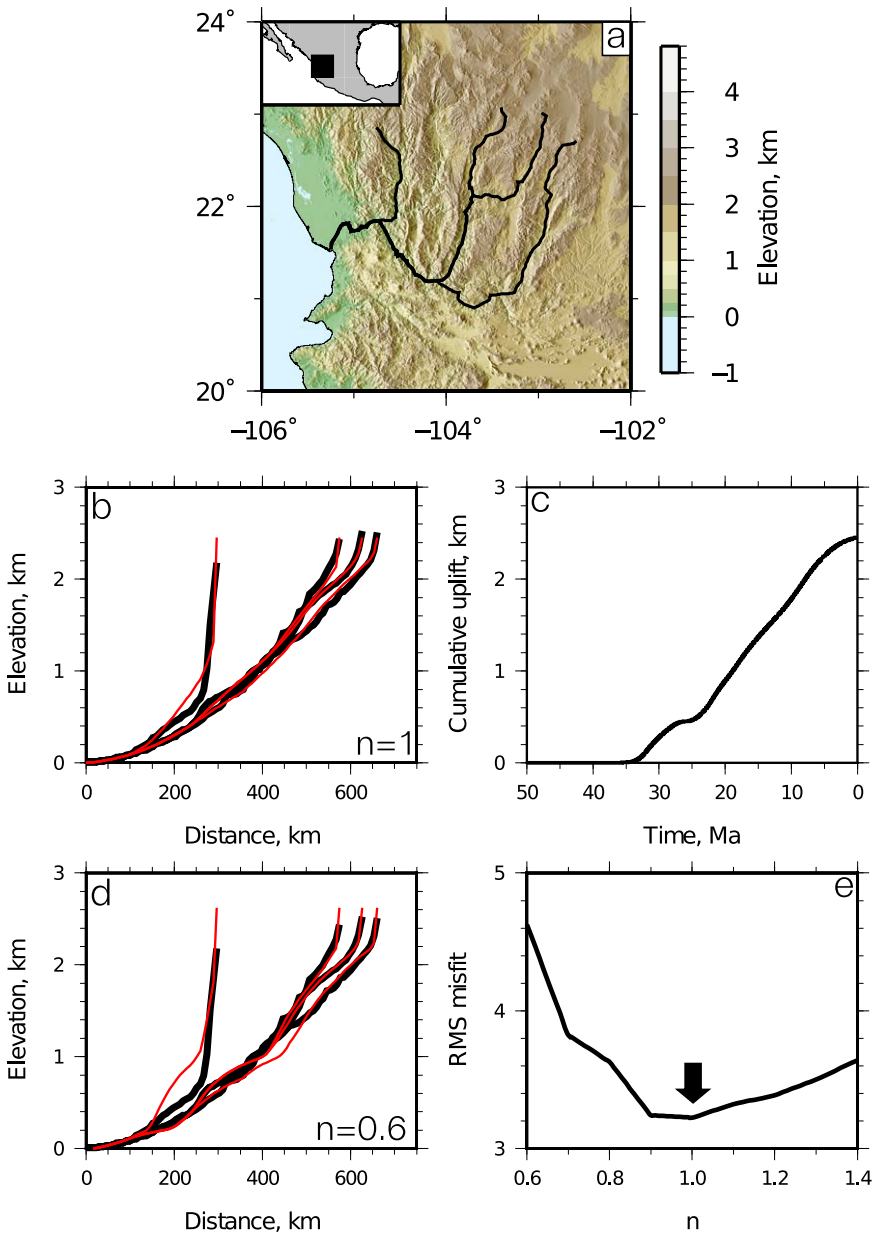

Figure 12. Testing effects of varying erosional parameter *n*. Joint inversion of four rivers from Rio Grande de Santiago catchment for $U(t)$. (a) Topographic map and location of four extracted river profiles. (b) Black lines = observed longitudinal profiles; red = best fitting theoretical profiles when $n = 1$, residual rms misfit = 3.23. (c) Calculated rock uplift history for rivers in (b). (d) Best fitting river profiles when $n = 0.6$, residual rms misfit = 6.07. (e) Residual misfit for sweep of *n* values. *n* was covaried with *v*. Note minimum misfit when $n = 1$ (arrow).

$$p(t) = p_\circ + S \sin(2\pi\omega t), \tag{10}$$

where $p_\circ$ and S are constants, such that $p(t) \geq 0$. ω denotes frequency. We inverted four rivers for uplift as a function of time using different precipitation rate histories (Figure 14). We tested scenarios in which precipitation rate varied with a period of 100 ka (i.e., eccentricity orbital perturbation) and two longer (~30 Ma) periods. In all cases, residual misfit is small, as is expected given the scaling relationship evident in equation (9). Within error, calculated uplift histories are indistinguishable when precipitation rate is constant or varies rapidly (i.e., 100 ka; cf. gray and red lines in Figure 14). These results indicate that rapid changes in discharge caused by ice loading and unloading since the Last Glacial Maximum will have a negligible effect on our results [see e.g., *Wickert et al.*, 2013]. Calculated uplift histories are distinguishable when precipitation rate varies with periods > 10 Ma (e.g., wet-dry-wet and dry-wet-dry cycles in Figure 14).

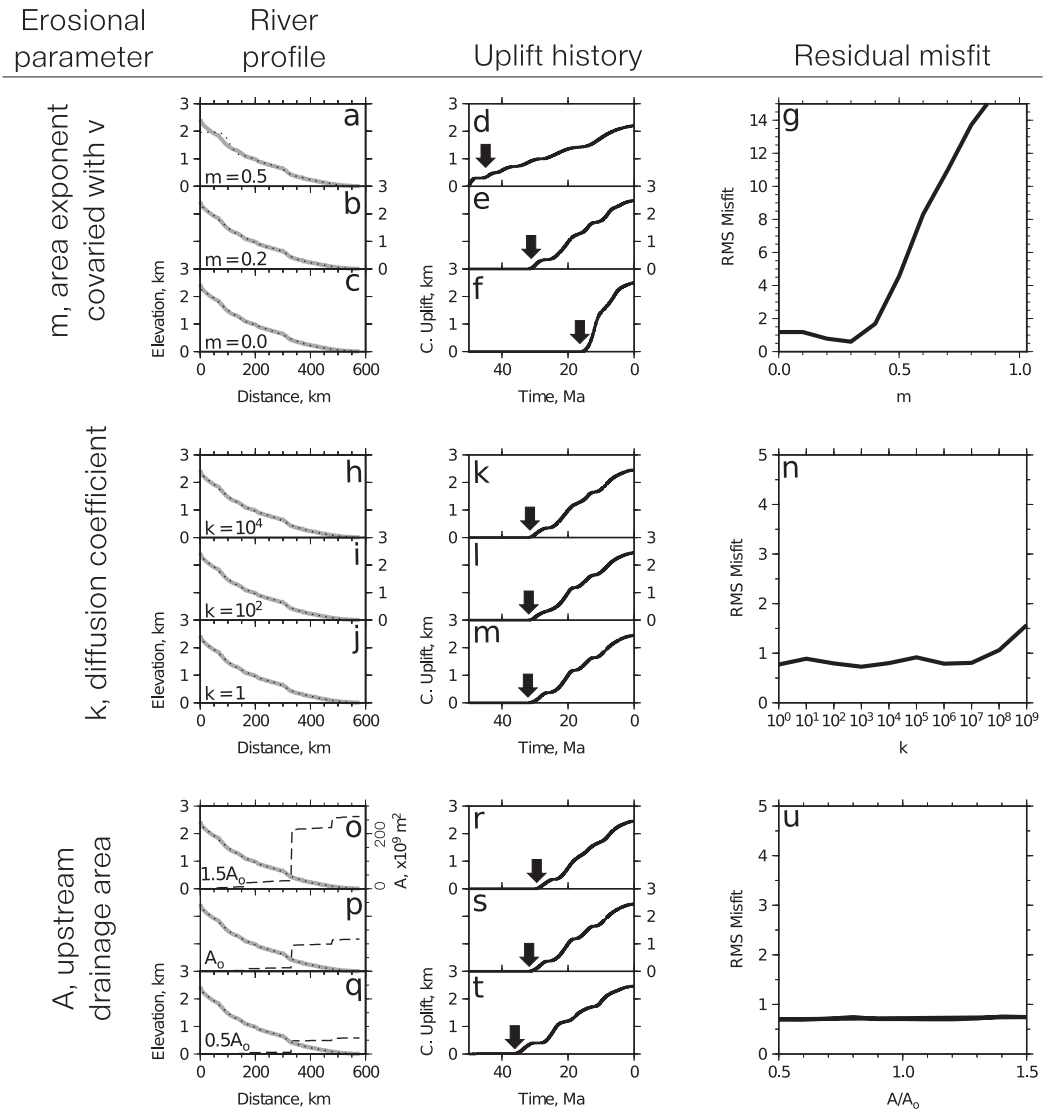

Figure 13. Testing effects of varying values of erosional parameters, v, m, κ, and A on calculated uplift and residual misfit. (a–c) Covarying v and m. Gray = observed river profile of Rio Grande de Santiago; dotted lines = best fitting theoretical profiles for $m = 0.5$, 0.2, and 0. (d–f) Cumulative rock uplift histories for values of erosional parameter shown in adjacent plots. Arrow = onset of uplift. (g) Residual rms misfit as a function of v and m. Note minimum misfit when $0.2 < m < 0.4$. (h–n) κ only has a significant effect on misfit when $\kappa > 10^8$ m^2/Ma. (o–u) Note that large uncertainties in A have a negligible effect on misfit.

Uplift rates have varied across North America as a function of both space and time [e.g., *Cather et al.*, 2012; *Roberts et al.*, 2012]. However, individual river profiles cannot be inverted for spatiotemporal variations in uplift rate because space and time trade-off (i.e., knickzones can be inserted upstream of river mouths). In the following section, we therefore exploit commonalities in the shapes of families of river profiles to invert for a spatiotemporal history of uplift.

5.3. Uplift as a Function of Space and Time

We jointly inverted 533 North American river profiles for a spatial and temporal history of uplift (Figure 15). To invert a drainage data set for a spatiotemporal history of uplift, a grid of uplift vertices, $U(x, y, t)$ is first defined. Uplift along individual rivers is bilinearly interpolated from surrounding vertices. During inversion, data and model misfit are minimized using a generalized version of the conjugate gradient method described in section 4.2. In this model, the first and second derivatives of uplift rate in space (x and y directions) and time are damped [e.g., *Roberts et al.*, 2013]. We tested models with different amounts of regularization (Figure 16). To reduce computational burden, we first ran a coarse model in which the spatial grid of uplift vertices had a spacing of 500 km. Results from this model were used as the starting solution for a

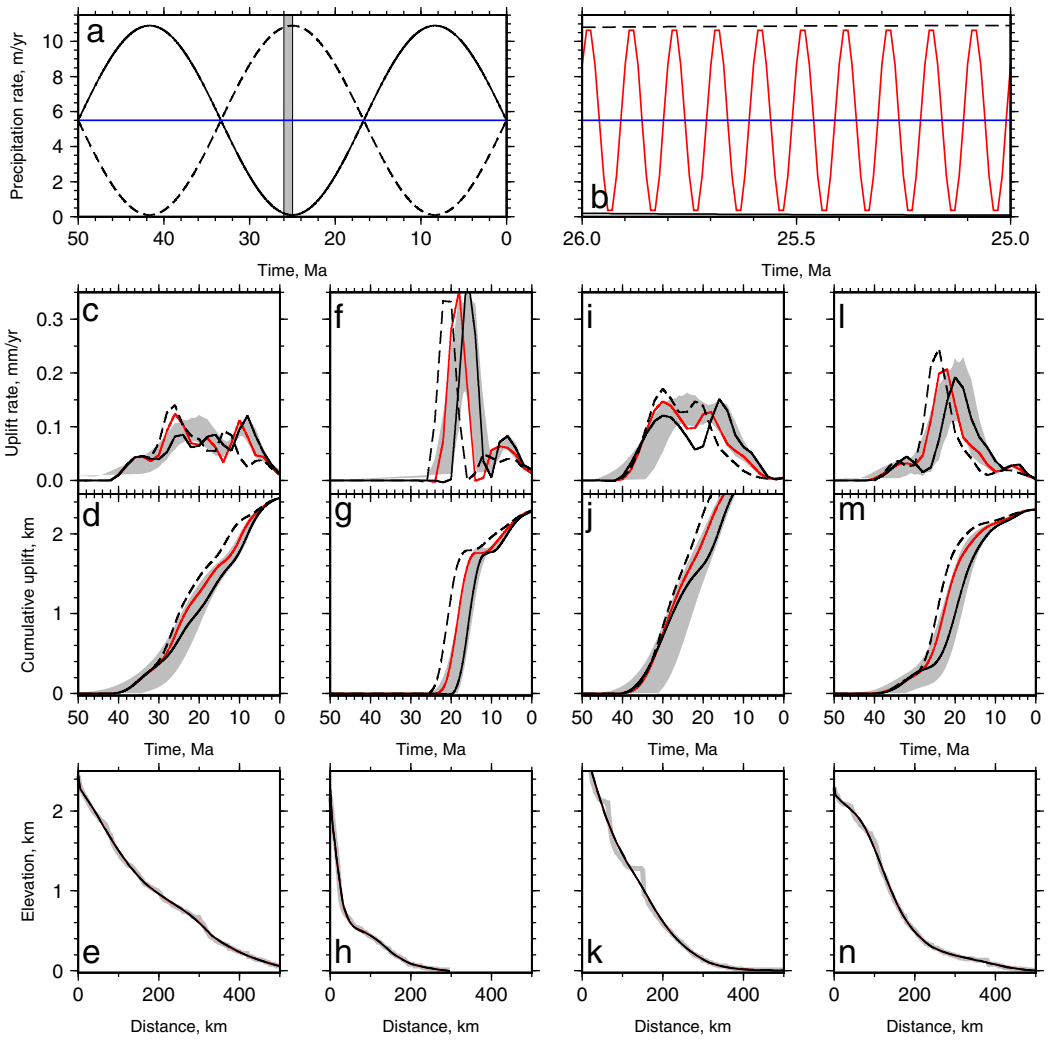

Figure 14. Precipitation rate tests. (a) Blue line = constant precipitation rate. Solid and dashed black lines = 50 Ma wet-dry-wet and dry-wet-dry cycles, respectively. (b) Zoom of gray box in Figure 14a showing 0.1 Ma precipitation rate variation. (c–d) Calculated rock uplift rate and cumulative rock uplift histories for Rio Grande de Santiago (Figure 8); gray band = results for constant precipitation rate (Figure 10). Colored lines correspond to precipitation rates in Figures 14a and 14b. (e) Gray line = observed river profile; colored lines = best-fitting theoretical river profiles for different precipitation rates. Note good fit for all tests. (f–h) Tributary of Rio Grande de Santiago. (i–k) Rio Panuco. (l–n) Rio Fuerte.

model with vertices spaced every 250 km. Temporal resolution = 5 Ma in both models. Model coverage is high since ~50 Ma when $m = 0.2$ and $v = 200$ m$^{0.6}$/Ma (Figure 9). In both models, spatial damping, $\mu \times w_S =$ 500 and temporal damping, $\mu \times w_T = 10^{-3}$. In the lower resolution model, rms misfit decreased from 41.69 to 10.97. In the higher-resolution model, residual rms misfit =7.61. Our results indicate western U.S. and Mexico were uplifting at a similar rate until ~25 Ma and that since ~25 Ma the Mexican Altiplano and the Trans-Mexican Volcanic Belt have been uplifted more rapidly. Calculated rock uplift is up to 4 km and maximum uplift rates are ~0.2 mm/yr. Highest rates of uplift were on the southwestern coast, Mexican Altiplano, and in the Trans-Mexican volcanic belt (Figure 17). The Colorado Plateau is predicted to have been uplifted by 1–1.5 km since ~40 Ma and eastern North America has been uplifted by a few hundred meters since 5 Ma (Figure 16). In the next section, we compare calculated uplift histories to independent estimates of uplift, erosion, and sedimentary flux.

6. Independent Constraints

We have calibrated erosional parameters using incision rate histories from rivers draining the Colorado Plateau and southwest Mexico. Our results indicate that western and central Mexico were uplifted at

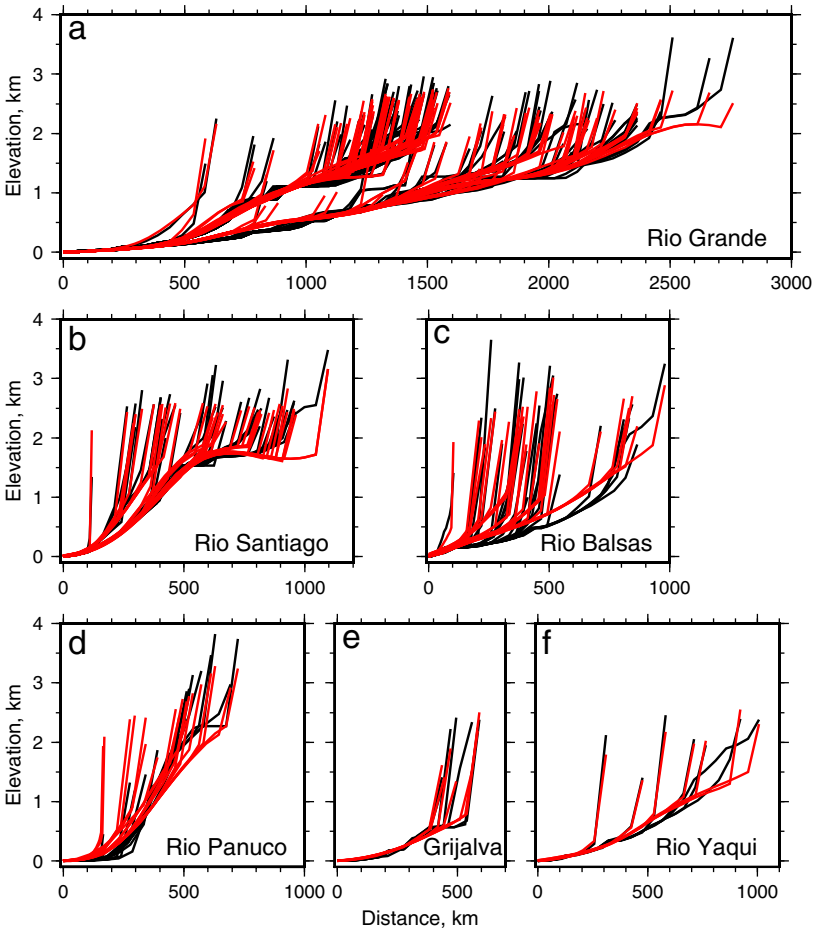

Figure 15. Inversion for uplift history using general optimization scheme. Black lines = observed river profiles grouped by catchment (Figure 7); red lines = best-fitting theoretical river profiles; residual rms misfit =7.61.

rates < 0.1 mm/yr until 25 Ma, which was followed by uplift rates of 0.15–0.2 mm/yr. During this time, western U.S. was uplifted at ~0.1–0.15 mm/yr. Southern Mexico and the trans-Mexican Volcanic Belt began uplifting earlier, but uplift also accelerated here from ~25 Ma. We now compare our calculated uplift and erosion histories to independent estimates of uplift, rock cooling, magmatism, and sedimentary flux.

6.1. Marine Terraces

Uplifted marine terraces are observed along the southwestern and eastern coasts of Mexico (Figure 6b). In Jalisco, southwest Mexico, marine notches at elevations of 1–5 m have radiocarbon ages of 0–1.3 ka, which implies rapid short-term uplift rates of 0.7–3.5 mm/yr [*Ramirez-Herrera et al*., 2004, 2010]. *Self* [1979] observed marine terraces in Veracruz, on the east coast of Mexico, but did not record their ages. On the eastern margin of the Yucatan peninsula, U-Th radiometric dating of coral topped marine terraces by *Blanchon et al*. [2009] indicates that uplift rates have been low (< 0.05 mm/yr) during the last 125 ka. Topographic swaths show that terraces in Veracruz have elevations of 10–70 m while the MIS 5e 125 ka marine terraces on the East Yucatan peninsula lie at less than 10 m (Figures 18a and 18b). We correlated observed and theoretical terrace heights with known glacial-interglacial sea-level variations, assuming that uplift rate has been constant during the last 125 ka (Figure 18c) [*Miller et al*., 2005]. The range of uplift rates we tested was 0–2 mm/yr. The uplift rate that results in the highest correlation between observed and calculated terraces in Veracruz is 0.51 mm/yr (Figures 18d and 18e). If uplift rate is lower or higher than 0.51 mm/yr, correlation between observed and calculated terraces decreases rapidly. Identical correlation exercises for other swath profiles, including marine terraces on the Yucautan peninsula, indicates that uplift rates decrease from West to East, consistent with the data of *Blanchon et al*. [2009] and our calculated history of uplift (Figure 18e).

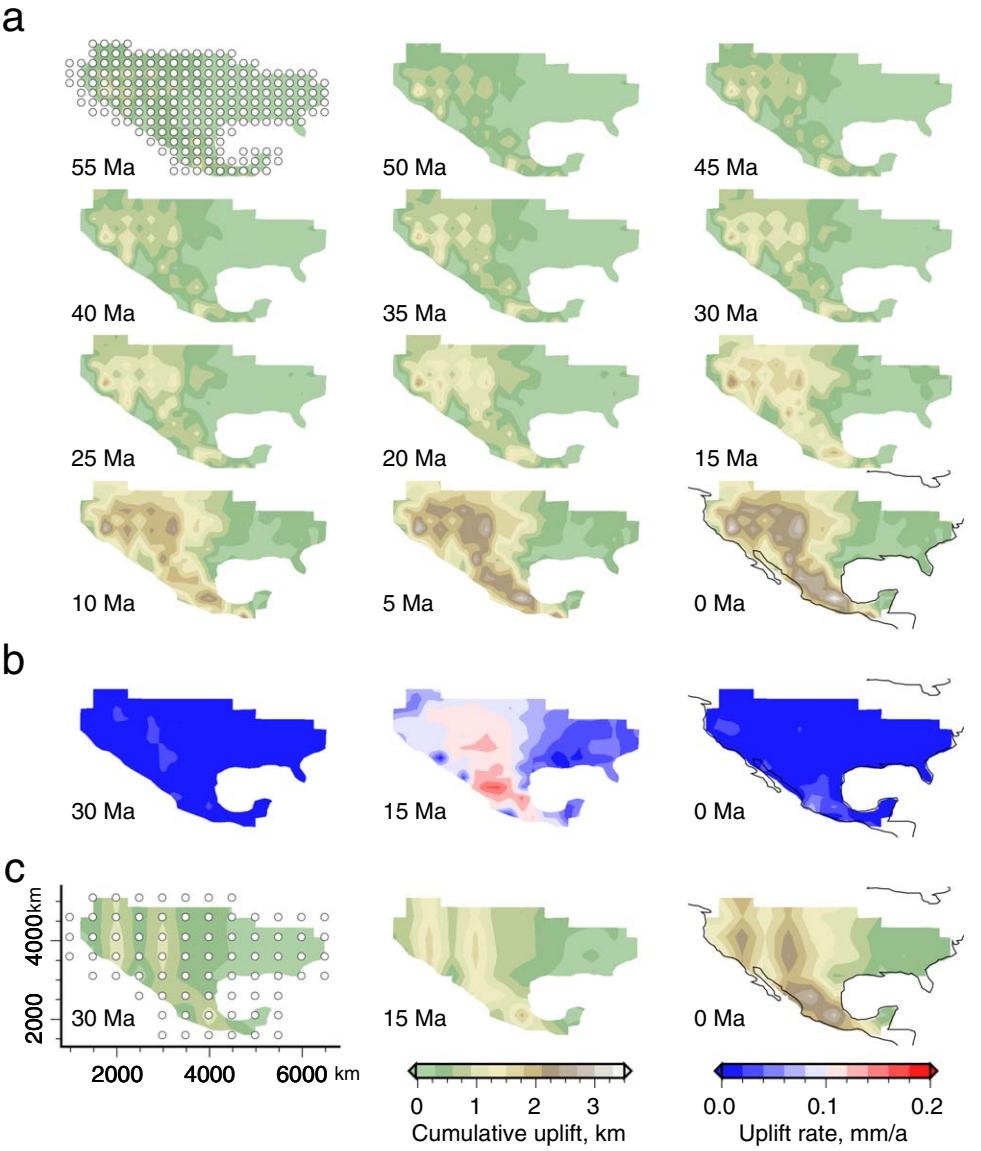

Figure 16. Inversion for rock uplift rate as a function of space and time [e.g., *Roberts et al*., 2012]. (a) Cumulative rock uplift, $\int_0^t U(x,y,t)\mathrm{d}t$. White circles = spatial distribution of uplift vertices: $\Delta x = \Delta y = 250$ km. (b) Calculated rock uplift rates, $U(x,y,t)$. (c) Smoother model: spatial distribution of uplift vertices $\Delta x = \Delta y = 500$ km.

6.2. Sedimentary Flux

A way to close the loop between uplift, erosion, and deposition of sediment is by predicting the sedimentary flux history of drainage networks. We test our results by comparing calculated efflux of eastward draining rivers to independent measurements of flux in the Gulf of Mexico [*Galloway et al*., 2011]. We assume that erosion is purely fluvial (i.e., we do not include hillslopes) and we do not separate solid and solute loads. For a single river, the total area of rock eroded, Q_s, as a function of time can be expressed as

$$Q_s(t) = \int_0^L -vA(x)^m \left(\frac{\partial z}{\partial x}\right)^n + \kappa \frac{\partial^2 z}{\partial x^2} \quad \mathrm{d}x, \tag{11}$$

where L is the length of the river. The area eroded from different rivers in a network can be integrated to determine sedimentary flux for a drainage basin. Using this approach, we estimate the sedimentary flux history for a network of 129 rivers, which flow into the western Gulf of Mexico. Model coverage is high from 40 to 0 Ma (Figure 9). During this time, calculated flux increases until 13 Ma and then decreases until present-day. These results are broadly consistent with *Galloway et al*. [2011]'s observations (Figure 19). We now

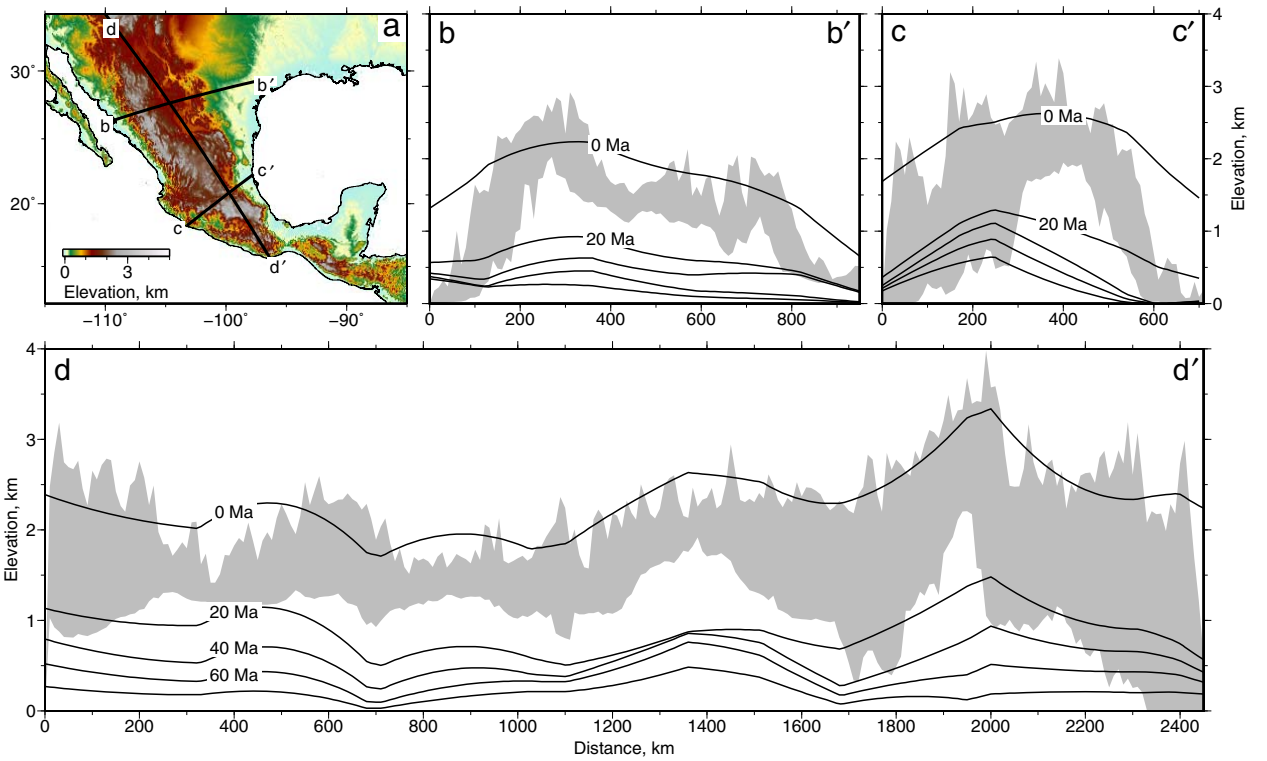

Figure 17. Isochrons of cumulative rock uplift (see Figure 16a). (a) Black = center of swaths. (b–d) Gray band = minimum and maximum topography in 100 km wide swath extracted from ETOPO1 data set. Black lines with labels = isochrons of calculated cumulative uplift; contour interval = 20 Ma.

compare calculated uplift and erosion histories to independent estimates of uplift and denudation across our study area.

6.3. Colorado and Rocky Mountain Plateaux

Cretaceous marine shales (e.g., the Mancos Formation), which crop out across the Colorado and Rocky Mountains plateaux, indicate that this region has been uplifted by up to ~3 km during the last 100 Ma (Figure 6) [e.g. *Sahagian*, 1987]. The timing of uplift and erosion during Cretaceous to Recent times is hotly debated [cf. *Flowers and Farley*, 2012; *Karlstrom et al*., 2014]. In Figures 20b–20d, we show our calculated uplift history and independent uplift and erosion histories. Our results indicate that the plateaux have been uplifted by up to 3 km since late Cretaceous times and that uplift rates were highest, 0.1–0.2 mm/yr, between 30 and 10 Ma (Figure 16). From ~40 Ma basaltic magmatism increased in New Mexico and its surroundings (Figure 20b) [*Fitton et al*., 1991; *Chapin et al*., 2004; www.navdat.org]. The history of sedimentary flux to the Gulf of Mexico and (U-Th)/He thermochronometry indicate that the Colorado and Rocky Mountains plateaux were denuded by 1–3 km during the last 80 million years (Figures 19 and 20c) [e.g., *Galloway et al*., 2011; *Flowers and Farley*, 2012; *Peyton and Carrapa*, 2013]. Figure 20d shows our calculated uplift history (solid and dashed black line) compared to the age of youngest marine sediments on the plateau, which are shown as a gray band [*Bond*, 1976; *Sahagian*, 1987; *Smith et al*., 1994]. Their mean modern elevation is shown as a black square in this figure. The depositional temperature of lacustrine sediments on the southern margin of the plateau has been by estimated using clumped isotope palaeothermometry [*Huntington et al*., 2010, brown line]. Combined with relief estimates from (U-Th)/He analyses by *Flowers et al.* [2008], these data indicate that the uplift and erosion history of the plateau was staged. Dynamic uplift estimated by converting mantle velocity anomalies to flow histories suggests that the plateau was uplifted by ~1 km during the last 35 Ma [*Moucha et al*., 2009, dotted line]. At approximately this time, the Chuska Erg, southern Colorado Plateau, was eroded by ~1.2 km [*Cather et al*., 2012, triangle]. The circles show the timing of up to 1.2 km of incision of "rim gravel" deposits on the margin of the plateau [*Elston and Young*, 1991]. These data suggest that the Colorado Plateau and its surroundings have been uplifted by 2–3 km since ~80 Ma and that uplift, and erosion, were staged, which corroborates our results.

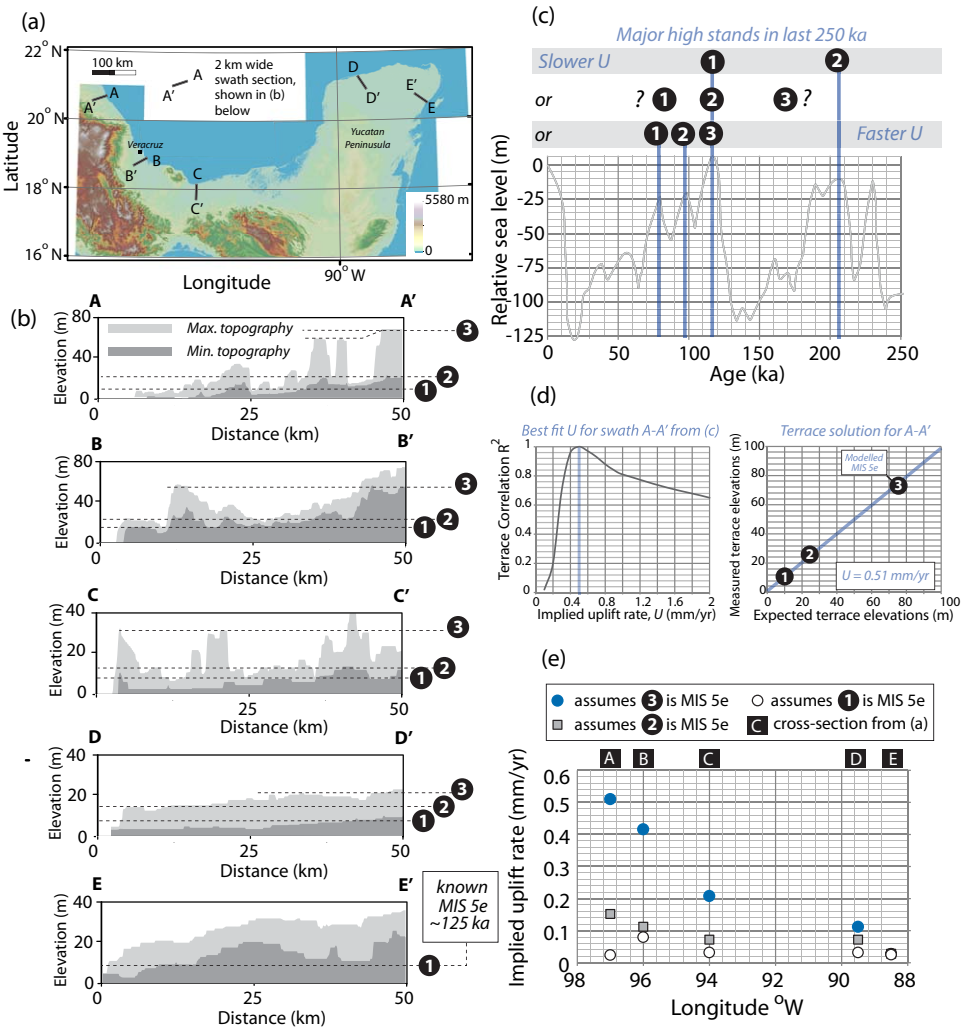

Figure 18. Coastal terraces in Mexico. (a) DEM showing location of 2 km wide swaths. (b) Topographic swaths; locations shown in Figure 18a. Labels ❶–❸ = likely marine terraces. Terrace at 7.5–9.5 m in swath E is ~125 ka [i.e., MIS 5e; *Blanchon et al.*, 2009]. (c) Sea level curve relative to present-day [*Miller et al.*, 2005]. Blue = marine high stands; correlation of terraces to high stands are shown above the graph. Slow uplift rates are implied if the lowermost terraces, labeled ❶, are correlated with MIS 5e. Faster uplift rates are implied if terrace level ❸ correlates with MIS 5e. (d) Left-hand plot shows correlation between observed and calculated terrace heights along swath A for range of constant uplift rates. Best-fitting uplift rate from 125–0 ka = 0.51 mm/yr (right-hand plot). (e) Implied uplift rate for all terraces shown in Figure 18b. Blue dots assume that terrace level ❸ is MIS 5e, which best-fits the data. Uplift rates assuming that terrace levels ❶ and ❷ are MIS 5e are shown for completeness as open circles and squares, respectively.

6.4. Big Bend National Park

In the Big Bend National Park, southern U.S., Cretaceous-Eocene rocks are unconformably overlain by sedimentary rocks that contain ~8 Ma old mammalian fossils [*Stevens and Stevens*, 2003]. *Cather et al.* [2012] suggest that up to 1 km of Eocene-Oligocene volcanic rocks have been eroded between these two units (Figure 20f, triangle). Pre-Oligocene and post-8 Ma deposition implies either slower uplift or subsidence during these time periods, which agrees with the calculated uplift history shown in Figure 20f.

6.5. Sierra Madre Oriental

At ~38 Ma, one of the largest ignimbrite provinces on Earth was starting to be built in western Mexico [*McDowell and Clabaugh*, 1979; *Ferrari et al.*, 1999, 2002, 2007]. This ignimbrite flare-up had two main phases [~32–28 Ma and 24–20 Ma; *Ferrari et al.*, 1999]. In the first phase, silicic sequences up to 1.5 km thick were emplaced across the Sierra Madre Occidental [*Ferrari et al.*, 2007]. In the second phase, magmatism was most intense at the southwestern edge of Sierra Madre Occidental (Figure 20a) [*Ferrari et al.*, 2012]. Apatite fission track analysis suggests that between 40 and 0 Ma, the Sierra Madre Oriental was eroded by 1–3 km [*Gray et al.*, 2003]. Apatite

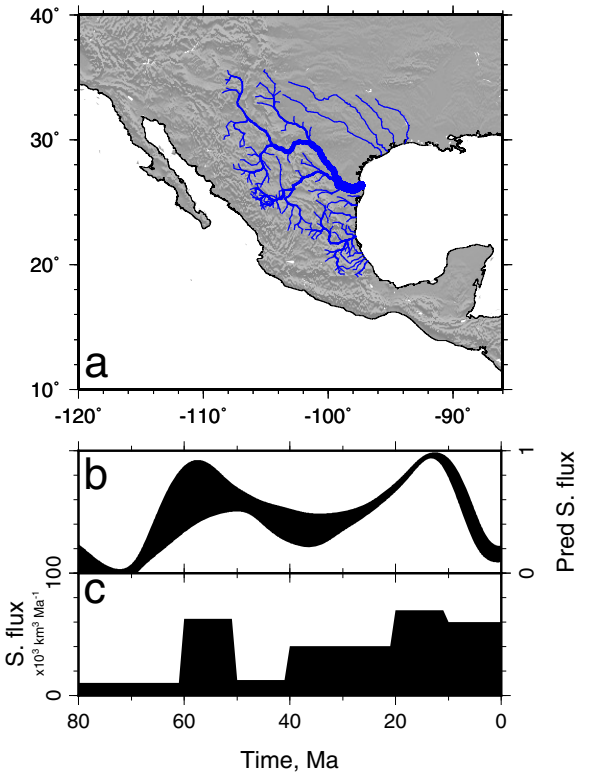

Figure 19. Comparison of predicted sedimentary flux to independent measurements. (a) Drainage map. Blue lines = 129 rivers used to calculate flux to western Gulf of Mexico. (b) Normalized predicted flux for uplift history shown in Figures 16a and 16b. Black band = range of flux when $0.1 \leq m \leq 0.4$ and $v = 4.16 \times 10^4 (2.78 \times 10^{-12})^m$. (c) Observed flux [*Galloway et al*., 2011]. Black bars = average flux in 10 Ma bins.

Helium (AHe) dating indicates that this region was exhumed rapidly at ~22 Ma, which is broadly coeval with a dramatic increase in calculated uplift rate at ~25 Ma (Figures 20h–20i) [*Gray et al*., 2003]. This uplift event coincided with extensive erosion, which created the Cretaceous-Miocene unconformity that *Cather et al*. [2008] identified in the Big Bend National Park. Calculated uplift rates in central and southern Mexico were high (0.1–0.2 mm/yr) during times of regional magmatism (Figure 20i). We tentatively suggest that regional magmatism has been generated by increased asthenospheric and lithospheric temperatures, which reduced the density of the lithosphere causing epeirogenic uplift during the last 40 Ma.

6.6. Jalisco

Holocene and Pleistocene uplifted marine terraces and wave-cut platforms are observed along the Jalisco coastline [section 6.1; *Ramirez-Herrera et al*. 2004, 2010]. Radiocarbon dating of emergent marine notches indicates that uplift rates during the last 1.3 ka have been rapid and variable: 0.7–3.5 mm/yr [*Ramirez-Herrera et al*. 2010]. Figures 20j and 20k show the calculated uplift history of southwest Mexico compared to the magmatic history of the region. The incision history of the ignimbrite surface requires 2 km of relief to have developed since 13 Ma, which suggests that topography was at least 2 km high during this time (Figure 20k, gray box) [*Montgomery and Lopez-Blanco*, 2003]. Inversion of drainage patterns indicates that at 40–20 Ma uplift and erosion rates increased. At approximately this time, plutonic rocks, which are now exposed at the surface, were emplaced along the southwest coast [*Moran-Zenteno et al*., 1996, K-Ar and Rb-Sr dating of 30 ±5 Ma]. Al_{tot} geobarometry of hornblendes indicates that these rocks were emplaced at depths of 13–20 km, which suggests that they were exhumed at rates of ~0.4−0.5 mm/yr [*Moran-Zenteno et al*., 1996]. Widespread erosion and exhumation since ~30 Ma is consistent with the erosion history estimated by inverting rivers draining Jalisco and is coeval with regional magmatism (Figure 20j).

7. Discussion

7.1. Dynamic Support

Our calculated uplift history suggests that central and western Mexico were uplifted by 2–3 km between 40 and 0 Ma, at rates of 0.05–0.2 mm/yr. The number of magmatic events increased throughout this time and today the average surface heat flux in this region is high: 90 ± 27 mW/m^2 (Figure 20) [*Smith et al*., 1979; *Ziagos et al*., 1985]. 50 km north of Mexico City surface heat flow is 83 ± 2 mW/m^2 and receiver functions indicate that the crust is 35 ± 5 km thick [*Ziagos et al*., 1985; *Perez-Campos et al*., 2008]. Solving the 1-D heat equation shows that the steady state geotherm for a lithosphere with a thermal conductivity of 2.5 W/m/°C, an asthenospheric temperature of 1360°C, and radiogenic heat production in the upper and lower crust of 2.5 and 2 μW/m^3, respectively, has a temperature of 750°C at

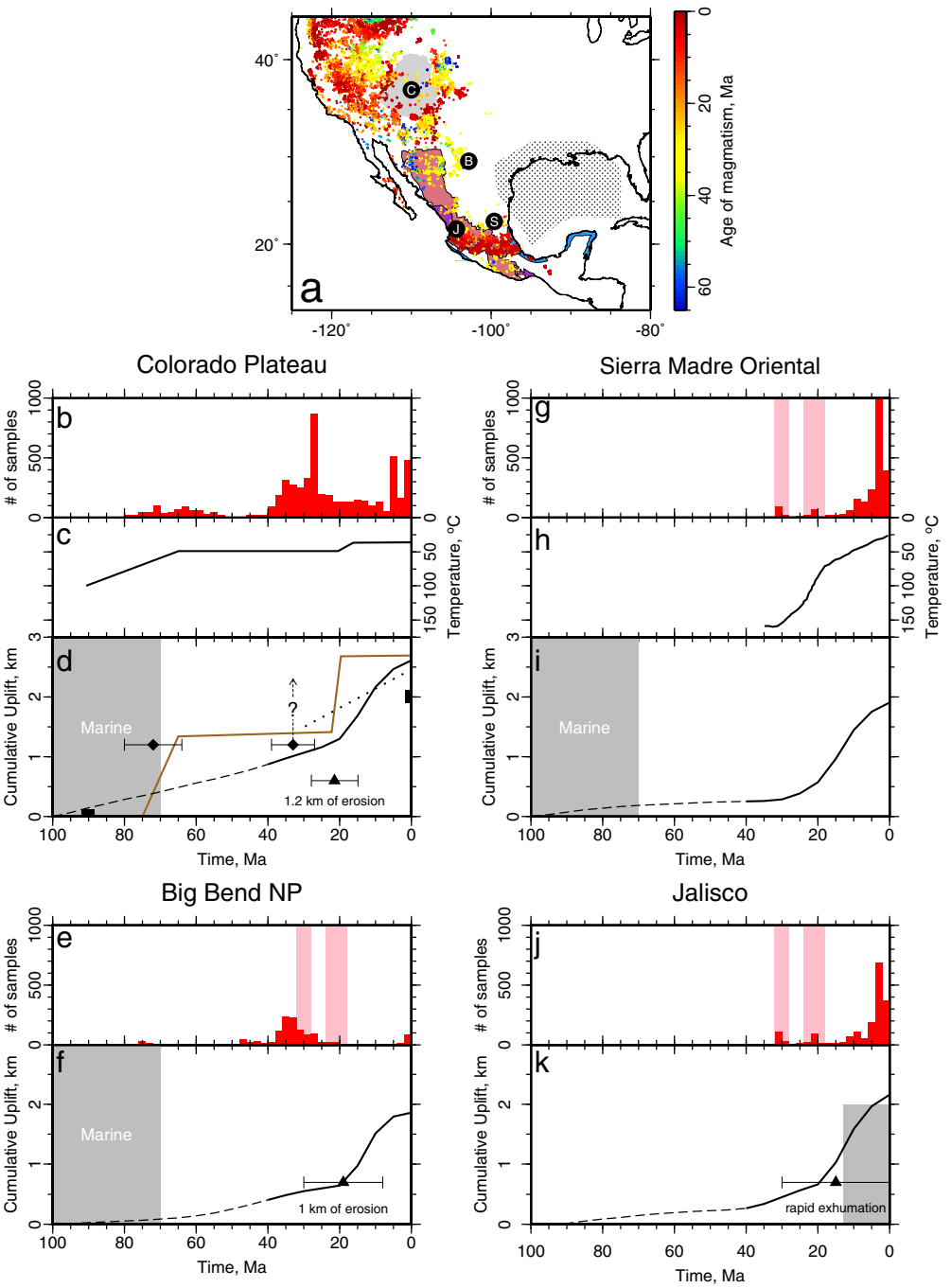

Figure 20. Independent uplift and denudation constraints compared to calculated rock uplift. (a) Gray polygon labeled C = Colorado Plateau; B = Big Bend National Park; S = Sierra Madre Oriental; J = Jalisco. Coloured circles = age of magmatism in Mexico and western North America; pink polygon = extent of Oligocene ignimbrites. Purple polygon = extent of Miocene ignimbrites. [*Ferrari et al.*, 1999; *Stevens and Stevens*, 2003; *Chapin et al.*, 2004; www.navdat.org]. Stippled pattern = extent of data set used to estimate sedimentary flux to the Gulf of Mexico [*Galloway et al.*, 2011]. Blue polygons = marine terraces [*Self*, 1979; *Ramirez-Herrera et al.*, 2010]. (b, g, e, j) Red histograms = 2 Ma bins of magmatic events within 5° of black circles in Figure 20a; pink bands = intense silicic magmatism [*Ferrari et al.*, 1999; *Chapin et al.*, 2004; *van Wijk et al.*, 2010; www.navdat.org]. (c) Black line = cooling history of basement at Upper Granite Gorge [*Flowers et al.*, 2008]. (d, f, i, k) Solid black line = calculated uplift history; dashed line = low model coverage. Gray-labeled polygon = marine conditions [see Figure 6; *Bond*, 1976; *Smith et al.*, 1994]. (d) Brown line = uplift history from clumped-isotope altimetry [*Huntington et al.*, 2010]; dotted line = dynamic uplift reconstructed from subplate flow [*Moucha et al.*, 2009]. Squares = uplift inferred from uplifted Cretaceous shorelines [*Sahagian*, 1987]; diamonds = minimum channel incision on Hualapai Plateau [*Eston and Young*, 1991]; triangle = 1.2 km of incision of Chuska erg [*Cather et al.*, 2008]. (f) Triangle = 1 km of regional erosion [*Stevens and Stevens*, 2003; *Cather et al.*, 2012]. (h) Black line = (U-Th)/He and AFT cooling history [*Gray et al.*, 2003]. (k) Gray box = minimum relief by 13 Ma from incision history of Jalisco coast [*Montgomery and Lopez-Blanco*, 2003]. Triangle = rapid exhumation of plutonic rocks [*Moran-Zenteno et al.*, 1996].

the base of the crust [*Turcotte and Schubert*, 2002; *McKenzie et al*., 2005]. This temperature estimate is consistent with petrologic analysis of exsolution lamellae in deep crustal xenoliths from central Mexico, which indicate that at ~40 Ma the lower crust was intruded by magmatic underplate, which has since cooled by 200–300° to ~800°C [*Hayob et al*., 1989]. High seismic velocities indicate that the lower crust beneath the Sierra Madre Occidental is dense, which is probably due to underplating [*Bonner and Herrin*, 1999]. The elastic model that best fits the admittance data requires a high internal load, which could be generated by Moho topography, and indicates the presence of underplating (Figure 4). Low seismic velocities in the asthenosphere, high surface heat flow and our admittance analysis suggest topography in Mexico is dynamically supported. The history of magmatism implies that this topography grew during the last 35 Ma. Several authors have suggested that Oligo-Miocene eruption of ignimbrites and coeval uplift of Mexico and western North America was caused by a change in the geometry of subducted plates and asthenospheric upwelling [e.g., *Humphreys et al*., 2003; *Ferrari et al*., 2012; *Cather et al*., 2012]. Our admittance calculations and calculated history of uplift indicate that these regions share a history of dynamic support, which generated 1–2 km of rock uplift during the last ~35 Ma.

8. Conclusions

Crustal thickness measurements and admittance calculations indicate that Mexico's topography is dynamically supported by up to 1 km. The shapes of Mexico's rivers contain temporal commonalities, which are nonlinear in space, that can be used to invert for a history of regional uplift. We extracted 533 longitudinal river profiles from the SRTM and ASTER GDEM data sets. This drainage inventory was jointly inverted for a spatial and temporal history of uplift. Erosional parameters were calibrated using the history of incision of lava dams along the Colorado river and of an ignimbrite surface in southwest Mexico. Results indicate that Mexico's topography grew during the last 40 Ma at a maximum rate of ~0.2 mm/yr. Calculated uplift and erosion histories are consistent with a broad range of independent incision, thermochronometric, and uplift data. We use our uplift and erosion model to predict sedimentary flux into the Gulf of Mexico during the last 50 Ma. We suggest that western North American topography grew in response to changing patterns of mantle convection during the last 40 million years and that longitudinal river profiles can indirectly record the history of dynamic support. High surface heat flow and the history of magmatism suggests that Mexico's topography has grown in response to magmatic underplating and asthenospheric upwelling.

Acknowledgments

G.G.R. was supported by an Imperial College London JRF. We thank N. White for providing advice and support, P. Allen, J. Paul, and J. Wilson for helpful discussion. Reviews by S. Jones and an anonymous person improved this manuscript. Digital elevation data was downloaded from http://gdem.ersdac.jspacesystems.or.jp and http://srtm.csi.cgair.org; geological maps from http://ngmdb.usgs.gov/gmna/; volcanic data from www.navdat.org.

References

Alzaga-Ruiz, H., M. Lopez, F. Roure, and M. Séranne (2009), Interactions between the Laramide Foreland and the passive margin of the Gulf of Mexico: Tectonics and sedimentation in the Golden Lane area, Veracruz State, Mexico, *Mar. Pet. Geol.*, *26*, 951–973.

Barra, F., J. Ruiz, V. A. Valencia, L. Ochoa-Landin, J. T. Chelsey, and L. Zurcher (2005), Laramide porphyry Cu-Mo mineralization in Northern Mexico: Age constraints from Re-Os geochronology in molybdenites, *Econ. Geol.*, *100*, 1605–1616.

Becker, J. J., et al. (2009), Global bathymetry and elevation data at 30 arc seconds resolution: SRTM30_PLUS, *Mar. Geod.*, *32*(4), 355–371.

Berlin, M. M., and R. S. Anderson (2007), Modeling of knickpoint retreat on the Roan Plateau, western Colorado, *J. Geophys. Res.*, *112*, F03S06, doi:10.1029/2006JF000553.

Bijwaard, M. D., and W. Spakman (2000), Non-linear global P-wave tomography by iterated linearized inversion, *Geophys. J. Int.*, *141*, 71–82.

Blanchon, P., A. Eisenhauer, J. Fietzke, and V. Liebetrau (2009), Rapid sea-level rise and reef back-stepping at the close of the last interglacial highstand, *Nature*, *458*, 881–884.

Bond, G. (1976), Evidence for continental subsidence in North America during the late Cretaceous global submergence, *Geology*, *4*, 557–560.

Bonner, J. L., and E. T. Herrin (1999), Surface wave studies of the Sierra Madre occidental of Northern Mexico, *Bull. Seismol. Soc. Am.*, *89*, 1323–1337.

Braile, L. W. (1989), Crustal structure of the Continental interior, *Memo. Geol. Soc. Am.*, *172*, 285–315.

Cather, S.M., S. D. Connell, R. M. Chamberlain, W. C. McIntosh, G. E. Jones, A. R. Potochnik, S. G. Lucas, and P. S. Johnson (2008), The Chuska erg: Paleogeomorphic and paleoclimatc implications of an Oligocene sand sea on the Colorado Plateau, *Geol. Soc. Am. Bull.*, *120*(1–2), 13–33.

Cather, S. M., C. E. Chapin, and S. A. Kelley (2012), Diachronous Episodes of Cenozoic erosion in southwestern North America and their relationship to surface uplift, palaeoclimate, palaeodrainage, and palaeoaltimetry, *Geosphere*, *8*(6), 1177–1206.

Chapin, C. E., M. Wilks, and W. C. McIntosh (2004), Space-time patterns of late-Cretaceous to present magmatism in New Mexico: Comparison with Andean volcanism and potential for future volcanism, *New Mex. Bur. Geol. Min. Resour.*, *160*, 13–40.

Cowie, P. A., M. Attal, G. E. Tucker, A. C. Whittaker, M. Naylor, A. Ganas, and G. P. Roberts (2006), Investigating the surface process response to fault interaction and linkage using a numerical modelling approach, *Basin Res.*, *18*, 231–266.

Daly, C., M. Halbleib, J. I. Smith, W. P. Gibson, M. K. Doggett, G. H. Taylor, J. Curtis, and P. P. Pasteris (2008), Physiographically sensitive mapping of climatological temperature and precipitation across the conterminous United States, *Int. J. Climatol.*, vol. 28, pp. 2031–2064, doi: 10.1002/joc.1688.

DiBiase, R. A., K. X. Whipple, A. M. Heimsath and W. B. Ouimet (2010), Landscape form and millennial erosion rates in the San Gabriel Mountains, *Earth Planet. Sci. Lett.*, *289*, 134–144.

Elston, D. P., and R. A. Young (1991), Cretaceous-Eocene (Laramide) landscape development and Oligocene-Pliocene drainage reorganization of transition zone and Colorado Plateau, Arizona, *J. Geophys. Res.*, *96*(B7), 12,389–12,406.
Ferrari, L. (2004), Slab detachment control on mafic volcanic pulse and mantle heterogeneity in central Mexico, *Geology*, *32*, 77–80.
Ferrari, L., M. Lopez-Martinez, G. Aguirre-Diaz, and G. Carrasco-Nunez (1999), Space-time patterns of cenozoic arc volcanism in Central Mexico: From the Sierra Madre occidental to the Mexican volcanic belt, *Geology*, *27*(4), 303–306.
Ferrari, L., C. M. Petrone, and L. Francalanci (2001), Generation of oceanic-island basalt-type volcanism in the western Trans-Mexican Volcanic Belt by slab rollback, asthenosphere infiltration and variable flux melting, *Geology*, *29*(6), 507–510.
Ferrari, L., M. Lopez-Martinez, and J. Rosas-Elgura (2002), Ignimbrite Flare-up and deformation in the Southern Sierra Madre occidental, Western Mexico: Implications for the late subduction history of the Farallon plate, *Tectonics*, *21*(4), doi:10.1029/2001TC001302.
Ferrari, L., M. Valencia-Moreno, and S. Bryan (2007), Magmatism and tectonics of the Sierra Madre occidental and its relation with the evolution of the Western margin of North America, *Geol. Soc. Am. Spec. Pap.*, *422*, 1–40.
Ferrari, L., T. Orozco-Esquivel, V. Manea, and M. Manea (2012), The dynamic history of the trans-Mexican volcanic belt and the Mexico subduction zone, *Tectonophysics*, *522–523*, 122–149.
Fitton, J. G., D. James, and W. P. Leeman (1991), Basic magmatism associated with Late Cenozoic extension in the western United States: Compositional variation in space and time, *J. Geophy. Res.*, *96*(B8), 13,693–13,711.
Flament, N., M. Gurnis, and R. D. Müller (2013), A review of observations and models of dynamic topography, *Lithosphere*, vol. 5, pp. 189–210, doi:10.1130/L245.1.
Flowers, R. M., and K. A. Farley (2012), Apatite ^{4}He/^{3}He and (U-Th)/He evidence for an ancient Grand Canyon, *Science*, *338*(1616), pp. 1616–1619, doi:10.1126/science.1229390.
Flowers, R. M., B. P. Wernicke, and K. A. Farley (2008), Unroofing, incision and uplift history of the southwestern Colorado plateau from apatite fission (U-Th)/He thermochronometry, *Geol. Soc. Am. Bull.*, *120*(5–6), 571–587.
Förste, C., et al. (2011), EIGEN-6: A new combined global gravity field model including GOCE data from the collaboration of GFZ—Potsdam and GRGS—Toulouse, *Geophys. Res. Abst.*, *31* (EGU General Assembly), EGU-3243-2.
French, S. W., K. M. Fischer, E. M. Syracuse, and M. E. Wysession (2009), Crustal structure beneath the Florida-to-Edmondton broadband Seismometer array, *Geophys. Res. Lett.*, *36*, L08309, doi:10.1029/2008GL036331.
French, S., V. Lekic, and B. Romanowicz (2013), Waveform tomography reveals channeled flow at the base of the oceanic asthenosphere, *Science*, *342*, 6155, pp. 227–230, doi:10.11126/science.1241514.
Galloway, W. E., P. E. Ganey-Curry, X. Li, and R. T. Buffler (2000), Cenozoic depositional history of the Gulf of Mexico basin, *AAPG Bull.*, *84*(11), 1743–1774.
Galloway, W. E., T. L. Whiteaker, and P. Ganey-Curry (2011), History of North American drainage basin evolution, sediment yield, and accumulation in the Gulf of Mexico basin, *Geosphere*, *7*(4), 938–973.
Gilbert, H. J., and A. F. Sheehan (2004), Images of crustal variations in the intermountain west, *J. Geophys. Res.*, *109*, B03306, doi:10.1029/2003JB002730.
Gilbert, H. J., A. F. Sheehan., K. G. Dueker, and P. Molnar (2003), Receiver functions in the western United States, with implications for upper mantle structure and dynamics, *J. Geophys. Res.*, *108*(B5), 2229, doi:10.1029/2001JB001194.
Goes, S., and S. van der Lee (2002), Thermal structure of the North American uppermost mantle inferred from seismic tomography, *J. Geophys. Res.*, *107*(B3), doi:10.1029/2000JB000049.
Gray, G. G., R. J. Pottorf, D. A. Yurewicz, K. I. Mahon, D. R. Pevear, and R. J. Chuchla (2003), Thermal and chromological record of Syn-Post Laramide Burial and Exhumation, Sierra Madre Oriental, Mexico. In *The Western Gulf of Mexico Basin: Tectonics, Sedimentary and Petroleum Systems*, edited by C. Bartoloni, R. T. Buffler, and A. Cantu-Chapa, *AAPG Mem*., 75(2001), 159–181.
Grand, S. P. (1994), Mantle shear structure beneath the Americas and surrounding oceans, *J. Geophys. Res.*, *99*(B6), 11591–11621.
Hack, J. T. (1957), Studies of longitudinal stream profiles in Virginia and Maryland, *U.S. Geol. Surv. Prof. Pap.*, *294B*, 45–80.
Hayob, J. L., E. J. Essene, J. Ruiz, F. Ortega-Guitierrez, and J. J. Aranda-Gomez (1989), Young high temperature granulites from the base of the crust in central Mexico, *Nature*, *342*, 265–268.
Howard, A. D., W. E. Dietrich, and M. A. Seidl (1994), Modeling fluvial erosion on regional to continental scales, *J. Geophys. Res.*, *99*(B7), 13,971–13,986.
Humphreys, E., E. Hessler, K. Dueker, L. Farmer, and E. Erslev (2003), How Laramide-age hydration by the Farallon slab controlled subsequent activity in the Western United States, *Int. Geol. Rev.*, *45*, 575–595.
Huntington, K. W., B. P. Wernicke, and J. M. Eiler (2010), The influence of climate change and uplift on the Colorado Plateau palaeotemperatures from carbonate clumped-isotope thermochronometry, *Tectonics*, *9*, TC3005, doi:10.1029/2009TC002449.
Jones, S. M., B. Lovell, and A. G. Crosby (2012), Comparison of modern and geological observations of dynamic support from mantle convection, *Q. J. Geol. Soc.*, *169*, 745–758, London, U. K.
Karlstrom, K. E., R. Crow, L. J. Crossey, D. Coblentz, and J. W. Van Wijk (2008), Model for tectonically driven incision of the younger than 6 Ma Grand Canyon, *Geology*, *36*(11), 835–838.
Karlstrom, K. E., et al. (2014), Formation of the Grand Canyon 5 to 6 million years ago through integration of older palaeocanyons, *Nat. Geosci.*, *7*, pp. 239–244, doi:10.1038/ngeo2065.
Kim, Y., R. W. Clayton, and F. Keppie (2011), Evidence of a collision between the Yucutan block and Mexico in the Miocene, *Geophys. J. Int.*, *187*, 989–1000.
Kirby, E., and K. Whipple (2001), Quantifying differential rock-uplift rates via stream profile analysis, *Geology*, *29*(5), 415–418.
Lague, D. (2014), The stream power river incision model: Evidence, theory and beyond, *Earth Surf. Processes Landforms*, *39*, pp. 38–61, doi:10.1002/esp.3462.
Li, A. K., K. M. Fischer, S. van der Lee, and M. E. Wysession (2002), Crust and upper mantle discontinuity structure beneath eastern North America, *J. Geophys. Res.*, *107*(B5), 2100, doi:10.1029/2001JB000190.
Liu, L., and M. Gurnis (2010), Dynamic subsidence and uplift of the Colorado plateau, *Geology*, *38*(7), 663–666.
Marquez, A., R. Oyarzun, M. Doblas, and S. P. Verma (1999), Alkalic (ocean-island basalt type) and calc-alkalic volcanism in the Mexican Volcanic belt: A case for plume-related magmatism and propagating rifting at an active margin? *Geology*, *27*(1), 51–54.
Meyer, D., et al. (2011), *ASTER Global Digital Elevation Model Version 2: Summary of Validation Results*, pp. 1–26, NASA Land Proc. Dist. Active Arch. Cent.
McDowell, F. W., and S. E. Clabaugh (1979), Ignimbrites of the Sierra Madre occidental and their relationship to the tectonic history of Western Mexico, In *Ash Flow Tuffs*, edited by C. E. Chapin and V. E. Elston, Spec. Pap. 180, pp. 113–124, Geol. Soc. of Am.
McKenzie, D. (2003), Estimating T_e in the presence of internal loads, *J. Geophys. Res.*, *108*(B9), 2438, doi:10.1029/2002JB001766.
McKenzie, D. (2010), The influence of dynamically supported topography on estimates of T_e, *Earth Planet. Sci. Lett.*, *295*, 127–138.

McKenzie, D. and D. Fairhead (1997), Estimates of the effective elastic thickness of the continental lithosphere from Bouguer and free air gravity anomalies, *J. Geophys. Res.*, *102*(B12), 27,523–27,552.
McKenzie, D., J. Jackson, and K. Priestley (2005), Thermal structure of oceanic and continental lithosphere, *Earth Planet. Sci. Lett.*, *233*, 337–349.
Melgar, D., and X. Perez-Campos (2010), Imaging the crust and subducted oceanic crust at the Isthmus of Tehuantepc, Mexico from receiver functions, *Pure Appl. Geophys.*, *168*, 1449–1460.
Miller, K. G., M. A. Kominz, J. V. Browning, J. D. Wright, G. S. Mountain, M. E. Katz, P. J. Sugarman, B. S. Cramer, N. Christie-Blick, and S. F. Pekar (2005), The Phanerozoic record of global sea-level change, *Science*, *310*, 1293–1298.
Montgomery, D. R., and J. Lopez-Blanco (2003), Post-Oligocene river Incision, Southern Sierra Madre occidental, Mexico, *Geomorphology*, *55*, 235–247.
Moran-Zenteno, D. J., P. Corona-Chavez, and G. Tolson (1996), Uplift and subduction erosion in Mexico since the Oligocene: Pluton geobarometry constraints, *Earth Planet. Sci. Lett.*, *141*(1–4), 51–56.
Moucha, R., A. M. Forte, D. B. Rowley, J. X. Mitrovica, N. A. Simmons, and S. P. Grand (2009), Deep mantle forces and the uplift of the Colorado plateau, *Geophys. Res. Lett.*, *36*, L19310, doi:10.1029/2009GL039778.
Pardo, M., and G. Suárez (1995), Shape of the subducted Rivera and Cocos plates in southern Mexico: Seismic and tectonic implications, *J. Geophys. Res.*, *100*(B7), 12,357–12,373.
Parker, R. L. (1994), *Geophysical Inverse Theory*, Princeton Univ. Press. Princeton, N. J.
Parrish, J. T., A. M. Ziegler, and C. R. Scotese (1982), Rainfall patterns and the distribution of coals and evaporites in the Mesozoic and Cenozoic, *Palaeogeog., Palaeoclimatol., Palaeoecol.*, *40*, 67–101.
Perez-Campos, X., Y. Kim, A. Husker, P. M. Davis, R. W. Clayton, A. Iglesias, J. F. Pacheco, S. K. Singh, V. C. Manea, and M. Gurnis (2008), Horizontal subduction and truncation of the Cocos plate beneath Central Mexico, *Geophys. Res. Lett.*, *35*, L18303, doi:10.1029/2008GL035127.
Perron, J. T., and L. Royden (2012), An integral approach to bedrock river profile analysis, *Earth Surf. Processes Landforms*, *38*, 570–576.
Persaud, P., X. Perez-Caampos, and R. W. Clayton (2007), Crustal thickness variations in the margins of the gulf of California from receiver functions, *Geophys. J. Int.*, *170*(2), 687–699.
Peyton, S. L., and B. Carrapa (2013), An overview of low-temperature thermochronology in the rocky mountains and its application to petroleum systems analysis, *AAPG Stud. Geol.*, *65*, 37–70.
Powell, M. J. D. (1964), An efficient method for finding the minimum of a function of several variables without calculating derivatives, *Comput. J.*, *7*(2), pp. 155–162, doi:10.1093/comjnl/7.2.155. [10.1093/comjnl/7.2.155][Match][16311326].
Priestley, K., and D. McKenzie (2006), The thermal structure of the lithosphere from shear wave velocities, *Earth Planet. Sci. Lett.*, *244*(1–2), 285–301.
Pritchard, D., G. G. Roberts, N. J. White, and C. Richardson (2009), Uplift histories from river profiles, *Geophys. Res. Lett.*, *36*, L24301, doi:10.1029/2009GL040928. [10.1029/2009GL040928][Match][16311326].
Ramirez-Herrera, M., V. Kostoglodov, and J. Urrutia-Fucugauchi (2004), Holocene-emerged notches and tectonic uplift along the Jalisco coast, Southwest Mexico, *Geomorphology*, *58*, 291–304.
Ramirez-Herrera, M., V. Kostoglodov, and J. Urrutia-Fucugauchi (2010), Overview of recent coastal tectonic deformation in the Mexican subduction zone, *Pure Appl. Geophys.*, *168*, 1415–1433.
Reed, J. C., J. O. Wheeler, B. E. Tucholke, W. R. Stettner, and D. R. Soller (2005), Decade of North American Geology, Geologic Map of North America, *Geol. Soc. Am*.
Righter, K. (1997), High bedrock incision rates in the Atenguillo River Valley, Jalisco, Western Mexico, *Earth Surf. Processes Landforms*, *22*(4), 337–343.
Righter, K., M. Caffee, J. Rossas-Elguera and V. Valencia (2010), Channel incision in the Rio Atenguillo, Jalisco, Mexico, defined by ^{36}Cl measurements of bedrock, *Geomorphology*, *120*(3–4), 279–292.
Ritsema, J., H. Van Heijst, and J. Woodhouse (2004), Global transition zone tomography, *J. Geophys. Res.*, *109*, B02302, doi:10.1029/2003JB002610.
Ritsema, J., A. Deuss, H. J. Van Heijst, and J. H. Woodhouse (2011), S40RTS: A degree-40 shear-velocity model for the mantle from new Rayleigh wave dispersion, teleseismic traveltime and normal-mode splitting function measurements, *Geophys. J. Int.*, *184*, 1223–1236.
Roberts, G. G., and N. J. White (2010), Estimating uplift rate histories from river profiles using African examples, *J. Geophys. Res.*, *115*, B02406, doi:10.1029/2009JB006692.
Roberts, G. G., N. J. White, G. L. Martin-Brandis, and A. G. Crosby (2012), An uplift history of the Colorado Plateau and its surroundings from inverse modelling of longitudinal river profiles, *Tectonics*, *31*, TC4202, doi:10.1029/2012TC003107.
Roberts, G. G., N. J. White, and B. Shaw (2013), An uplift history of Crete, Greece, from inverse modeling of longitudinal river profiles, *Geomorphology*, *198*, 177–188.
Roe, G., D. Montgomery, and B. Hallet (2002), Effects of orographic precipitation variations on the concavity of steady-state river profiles, *Geology*, *30*, 143–146.
Rosenbloom, N. A., and R. S. Anderson (1994), Hillslope and channel evolution in a marine terraced landscape, Santa Cruz, California, *J. Geophys. Res.*, *99*(B7), 14,013–14,029.
Sahagian, D. (1987), Epeirogenic and eustatic sea level changes as inferred from Cretaceous shoreline deposits: Applications to the central and western United States, *J. Geophys. Res.*, *9*(B6), 4895–4904.
Self, R. P. (1979), Longshore variations in beach sands, Nautla area, Veracruz, Mexico, *J. Sediment. Res.*, *47*(4), 1437–1443.
Sheehan, A. F., G. A. Abers, C. H. Jones, and A. L. Lerner-Lam (1995), Crustal thickness variations across the Colorado rocky mountains from teleseismic receiver functions, *J. Geophys. Res.*, *100*(B10), 20,391–20,404.
Shelef, E. and G. E. Hilley (2014), Symmetry, randomness, and process in the structure of branched channel networks, *Geophys. Res. Lett.*, *41*, 3485–3493, doi:10.1002/2014GL059816.
Smith, A. G., D. G. Smith, and B. M. Funnell (1994), *Atlas of Mesozoic and Cenozoic Coastlines*, Cambridge Univ. Press, Cambridge.
Smith, D. L., C. E. Nuckels, R. L. Jones, and G. A. Cook (1979), Distribution of heat flow and radioactive heat generation in northern Mexico, *J. Geophys. Res.*, *84*(B5), 2371–2379.
Snelson, C. M., T. J. Henstock, G. R. Keller, K. C. Miller, and A. Levander (1998), Crustal and upper mantle structure and upper mantle structure along the deep probe seismic profile, *Rock. Mt. Geol.*, *33*, 181–198.
Spasojevic, S., L. Liu, M. Gurnis, and D. R. Müller (2008), The case for dynamic subsidence of the U.S. East coast since the Eocene, *Geophys. Res. Lett.*, *35*, L08305, doi:10.1029/2008GL033511.

Stevens, M. S., and J. B. Stevens (2003), Carnivora (Mammalia, Felidae, Canidae, and Mustelidae) from the earliest Hemphillian Screw Bean local fauna, Big Bend National park, Brewster County, Texas, *Am. Mus. Nat. Hist. Bull.*, *279*, 177–211.

Stock, J. D., and D. R. Montgomery (1999), Geological constraints on bedrock river incision using the stream power law, *J. Geophys. Res.*, *104*(B3), 4983–4993.

Suter, M. (1984), Cordilleran deformation along the eastern edge of the Valles-San Luis Potosi carbonate platform, Sierra Madre Oriental fold-thrust belt, East-Central Mexico, *Geol. Soc. Am. Bull.*, *95*, 1387–1397.

Suter, M., M. L. Martínez, O. Q. Legorreta, and M. C. Martínez (2001), Quaternary intra-arc extension in the central Trans-Mexican volcanic belt, *GSA Bull.*, *113*(6), 693–703.

Tapley, B., J. Ries, S. Bettadpur, D. Chambers, M. Cheng, F. Condi, B. Gunter, Z. Kang, P. Nagel, and R. Pastor (2005), GGM02: An improved Earth gravity field model from GRACE, *J. Geod.*, *79*(8), 467–468.

Turcotte, D. L., and G. Schubert (2002), *Geodynamics*, 2nd ed., Cambridge Univ. Press, N. Y.

Van Wijk, J. W., W. S. Baldridge, J. van Huenen, S. Goes, R. Aster, D. D. Coblentz, S. P. Grand, and J. Ni (2010), Small-scale convection at the edge of the Colorado plateau: Implications for topography, magmatism and evolution of proterozoic lithosphere, *Geology*, *38*(7), 611–614.

Whipple, K. X. (2001), Fluvial landscape response time: How plausible is steady-state denudation?, *Am. J. Sci.*, *301*, 313–325.

Whipple, K. X., and G. E. Tucker (1999), Dynamics of the stream-power river incision model: Implications for height limits of mountain ranges, landscape response timescales, and research needs, *J. Geophys. Res.*, *104*(B8), 17,661–17,674.

Whipple, K. X., and G. E. Tucker (2002), Implications of sediment-flux-dependent river incision models for landscape evolution, *J. Geophys. Res.*, *107*(B2), doi:10.1029/2000JB000044.

Whittaker, A. C., and S. J. Boulton (2012), Tectonic and climatic controls on knickpoint retreat rates and landscape response times, *J. Geophys. Res.*, *117*, F02024, doi:10.1029/2011JF002157.

Whittaker, A. C., P. A. Cowie, M. Attal, G. E. Tucker, and G. P. Roberts (2007), Contrasting transient and steady-state rivers crossing active normal faults: New field observations from the Central Apennines, Italy, *Basin Res.*, *9*, 529–556.

Wickert, A. D., J. X. Mitrovica, C. Williams, and R. S. Anderson (2013), Gradual demise of a thin southern Laurentide ice sheet recorded by Mississippi drainage, *Nature*, *502*, 668–671.

Willett, S. D., S. W. McCoy, J. T. Perron, L. Goren, and C.-Y. Chen (2014), Dynamic Reorganization of River Basins, *Science*, *343*(6175), doi: 10.1126/science.1248765.

Wilson, D. C., R. Aster, J. Ni, S. Grand, M. West, W. Gao, W. S. Baldridge, and S. Semken (2005), Imaging the seismic structure of the crust and upper mantle beneath the Great Plains, Rio Grande Rift, and Colorado Plateau using receiver functions, *J. Geophys. Res.*, *110*, B05306, doi:10.1029/2004JB003492.

Witt, C., S. Brichau, and A. Carter (2012), New constraints on the origin of the Sierra Madre de Chiapas (South Mexico) from sediment provenance and apatite thermochronometry, *Tectonics*, *31*, TC6001, doi:10.1029/2012TC003141.

Zachos, J., M. Pagani, L. Sloan, E. Thomas, and K. Billups (2001), Trends, rhythms, and aberrations in global climate 65 Ma to present, *Science*, *292*(686), pp. 686–693, doi:10.1126/science.1059412.

Ziagos, J. P., D. D. Blackwell, and F. Mooser (1985), Heat flow in southern Mexico and the thermal effects of subduction, *J. Geophys. Res.*, *90*(B7), 5410–5420.